

https://dspace.org/

Effects of hydrostatic internal pressure upon the buckling of hollow sections subject to axial compression

Tansley, Kelby John

2020
https://hdl.handle.net/10539/31193

Downloaded from a DSpace repository. https://dspace.org/

Effects of Hydrostatic Internal Pressure upon the Buckling of Hollow Sections subject to Axial Compression

Table of Contents

Abstract 1

Introduction 2

Background 3

- Related Investigations 3
- Elastic Global Buckling of Columns 4
- Elastic and Plastic Local Buckling of Columns 6
- Physical Imperfections of Hollow Sections 7
  - Perturbed Theoretical Equations 9

Numerical Experiment Setup 11

- Hollow Section Geometry 11
- Applied Loads and Boundary Conditions 11
- Material Properties 12
- Finite Element Method (FEM) 13
  - FEM Elements 14
- Modelling Hollow Sections 15
- Modelling Imperfections 15
  - Initial out of straightness 16
  - Initial out of width or diameter 16
- Modelling Applied Loads and Boundary Conditions 19

Experiment Dataset 20

- Convergence Study 20
  - Typical Converged Mesh 23

Results 24

- Circular Hollow Sections (CHS) 24
  - Perfect Models 24
  - Out of Straightness (OOS) 27
  - Out of Diameter (OOD) 30
- Square Hollow Section (SHS) 34

Perfect Models 34
Out of Straightness (OOS) 37
Out of Width (OOW) 39
Discussion 41
Circular Hollow Section 41
Out of Straightness 42
Out of Diameter 42
Square Hollow Section (SHS) 43
Out of Straightness 44
Out of Width 44
Conclusion 45
Suggestions for Future Work 47
References 48

List of Figures

Figure 1: Simple column 5
Figure 2: Graph of mean buckling stress versus slenderness ratio of a column 6
Figure 3: Schematic of out-of-roundness imperfections in CHS 7
Figure 4: SHS concave and convex imperfection 8
Figure 5: Out-of-straightness imperfection of CHS and SHS 8
Figure 6: Elephant foot buckling half wavelength, Lq 9
Figure 7: Typical graph of stress vs slenderness ratio for straight and curved columns under axial compression 10
Figure 8: Dimensions for Circular and Square Hollow Sections 11
Figure 9: Diagram of loaded CHS and SHS under Fixed Roller (FR) and Pinned Roller (PR) boundary conditions 12
Figure 10: Quadrilateral plate element types 14
Figure 11: Perfect square and circular hollow FEM model 15
Figure 12: Annotations of out of straightness imperfection of CHS and SHS models 16
Figure 13: Out of straightness model of CHS and SHS 16
Figure 14: Peak amplitude of out of diameter sinusoidal imperfection in circular sections 17
Figure 15: Peak amplitude of out of width sinusoidal imperfection in Square sections 18
Figure 16: Out of diameter CHS perturbed with **4** sine waves 18
Figure 17: Out of diameter CHS perturbed with **6** sine waves 18
Figure 18: 0.5 Theta SHS Perturbation 18
Figure 19: CHS end as rigid links 19
Figure 20: SHS end as rigid links 19
Figure 21: Finite element model of loaded circular and square hollow section 19
Figure 22: Convergence charts of CHS data set, for upper and lower D/t and L/r ratios 21
Figure 23: Convergence charts of SHS data set, for upper and lower D/t and L/r ratios 22
Figure 24: Converged 285mm by 1m SHS 23
Figure 25: Converged 700mm by 1m SHS 23
Figure 26: Converged 324mm by 1m CHS 23

Figure 27: Converged 700mm by 1m CHS 23
Figure 28: Perfect CHS, pinned roller with axial force only 24
Figure 29: Perfect CHS, pinned roller with axial force & internal pressure 24
Figure 30: Perfect CHS, fixed roller with axial force only 25
Figure 31: Perfect CHS, fixed roller with axial force & internal pressure 25
Figure 32: Typical global buckling mode shape of perfect CHS for fixed roller and pinned roller BC 25
Figure 33: CHS typical local buckling mode shapes for perfect model 25
Figure 34: CHS local buckling mode shapes. Numbers represent the number of sine waves seen along the circumference. 26
Figure 35: Local Buckling zone with sine wave count of perfect CHS, fixed roller with axial force only . 26
Figure 36: Local Buckling zone with sine wave count of perfect CHS, fixed roller with axial force & internal pressure 26
Figure 37: 0.3% out of straightness CHS, pinned roller with axial force only 27
Figure 38: 0.3% out of straightness CHS, pinned roller with axial force & internal pressure 27
Figure 39: 0.3% out of straightness CHS, FR with axial force only 28
Figure 40: 0.3% out of straightness CHS, FR with axial force & internal pressure 28
Figure 41: Local Buckling with sine wave count of out of straightness CHS, fixed roller with axial force only 28
Figure 42: Local Buckling with sine wave count and crippling zones of out of straightness CHS, fixed roller with axial force & internal pressure 28
Figure 43: Crippling of shorter side of out of straightness CHS, at centre of member 29
Figure 44: Crippling of shorter side of out of straightness CHS, at toe of member with fixed roller boundary condition only 29
Figure 45: Out of diameter CHS perturbed with **4** sine waves 30
Figure 46: Out of diameter CHS perturbed with **6** sine waves 30
Figure 47: 3% out of diameter CHS, 4 sine waves, pinned roller with axial force only 30
Figure 48: 3% out of diameter CHS, 4 sine waves, pinned roller with axial force & internal pressure ... 30
Figure 49: 3% out of diameter CHS, 4 sine waves, fixed roller with axial force only 31
Figure 50: 3% out of diameter CHS, 4 sine waves, fixed roller with axial force & internal pressure 31
Figure 51: Local Buckling sine wave count of CHS 3% out of diameter with 4 sine waves, fixed roller and axial force only 32

Figure 52: Local Buckling sine wave count of CHS 3% out of diameter with 4 sine waves, fixed roller, axial force and internal pressure 32
Figure 53: 3% out of diameter CHS, 6 sine waves, pinned roller with axial force only 32
Figure 54: 3% out of diameter CHS, 6 sine waves, pinned roller with axial force & internal pressure ... 32
Figure 55: 3% out of diameter CHS, 6 sine waves, fixed roller with axial force only 33
Figure 56: 3% out of diameter CHS, 6 sine waves, fixed roller with axial force & internal pressure 33
Figure 57: 3% out of diameter CHS, 6 sine waves, fixed roller with axial force only 33
Figure 58: 3% out of diameter CHS, 6 sine waves, fixed roller with axial force & internal pressure 33
Figure 59: Perfect SHS, pinned roller with axial force only 34
Figure 60: Perfect SHS, pinned roller with axial force and internal pressure 34
Figure 61: Cross-section of typical locally buckled SHS 34
Figure 62: Perfect SHS, fixed roller with axial force only 35
Figure 63: Perfect SHS, fixed roller with axial force and internal pressure 35
Figure 64: Typical Local buckling mode shapes of perfect SHS for various W/t and L/W ratios 35
Figure 65: Typical global buckling mode shape of perfect SHS for fixed roller and pinned roller 35
Figure 66: Local Buckling of perfect SHS, FR axial force only 36
Figure 67: Local Buckling of perfect SHS, FR axial force & internal pressure 36
Figure 68: 0.3% out of straightness SHS, pinned roller with axial force only 37
Figure 69: 0.3% out of straightness SHS, pinned roller with axial force & internal pressure 37
Figure 70: 0.3% out of straightness SHS, FR with axial force only 37
Figure 71: 0.3% out of straightness SHS, FR with axial force & internal pressure 37
Figure 72: Local buckling of typical perfect SHS with axial force only 38
Figure 73: Local buckling of typical out of straightness SHS, with axial force & internal pressure 38
Figure 74: Cross-section of typical out of straightness SHS showing a higher amplitude on the shorter face of the member 38
Figure 75: 2% out of width SHS, PR with axial force only 39
Figure 76: 2% out of width SHS, PR with axial force & internal pressure 39
Figure 77: 2% out of width SHS, FR with axial force only 39
Figure 78: 2% out of width SHS, FR with axial force & internal pressure 39
Figure 79: Local buckling zone of 2% out of width Class 4 SHS, fixed roller with axial force only 40

Figure 80: Local buckling zone of 2% out of width Class 4 SHS, fixed roller, with axial force and internal pressure 40
Figure 81: Toe buckling zone for out of width SHS 40
Figure 82: Cross-section of toe buckling zone for out of width SHS 40

List of Tables

Table 1: Table of allowable imperfections for circular and square hollow sections to ISO-657-14 9
Table 2: Experiment dataset for Circular and Square Hollow Sections 20

Abstract

A linear finite element buckling analysis of simply and fixed to roller supported structural steel circular and square hollow sections are presented in this investigation. The closed-end sections with perfect and imperfect cross-sections showed comparisons to the Euler buckling curve for both the axial force only and the axial force and internal pressure load cases. Section classification according to Eurocode 3 (Eurocode-3, 2005) revealed a data set including all 4 classes and an expanded class 4 set tending towards thin shell ratios. The circular hollow sections showed high reductions in strength with sine wave perturbations along the circumference, where six and four sinusoidal waves were the greatest reducers in strength. The internal pressure showed a steady increase in strength for all class 4 sections with no influence on class 1 to 3 sections. The mean buckling stress was greater than the yield stress of steel even with perturbation amplitudes outside the Eurocode limits. However, this was not true for square hollow sections. The perfect mesh was weaker than the perturbed mesh for all local and global buckling modes. Cross-sectional and global perturbation increased the mean buckling stress for all classes of square hollow sections. Class 1 to 3 sections all buckled above yield stress while all class 4 sections buckled before the material yield point. The internal pressure had a negligible increase in strength for all classes. However, a strength reduction was seen with a larger width to thickness and length to radius of gyration ratios when cross-sectional perturbation was considered. For both the square and circular sections, the out of straightness theoretical curves showed no benefit as all class 1 to 3 sections revealed buckling strengths greater than the Euler curve and the yield stress point.

Keywords: Circular hollow section; Square hollow section; Axial compressive buckling; Hydrostatic internal pressure; Buckling theory; Linear buckling; Finite-element method; Initial imperfection; Section classification

Introduction

Hollow steel sections are versatile and are one of the most efficient forms of structural elements. They have a large second moment of inertia and a high torsional stiffness which results in a high bending and torsional strength for their lightweight.

The motion of Structural Engineering globally tends towards lighter, cheaper structures. Engineers have looked to expand upon the efficiencies of hollow sections and have considered composite actions such as reinforced surfacing, added infill, elements within elements etc. When steel structures are loaded in compression, their strength is limited by buckling. This buckling is often catastrophic and a reliable prediction of the buckling strength of these sections is a strong aspiration for engineers.

Euler's investigation of the elastic stability of slender columns paved the way for the development of the theory of elastic buckling of structures. The governing equations of the problem are linearized, and the resulting eigenvalue problem yields the buckling loads as eigenvalues and the corresponding modes as eigenvectors.

A parametric study of the buckling of hollow sections is made whereby the length and diameter or width of the section are varied. The internal pressure (being a function of the height of element) is applied with two boundary conditions considered. The results of a perfect and imperfect structure are compared with theoretical results.

The local buckling strength effect of internal pressure in a hollow section of a circular and square profile is enhancing for a diameter to thickness ratio less than 150 and a width to thickness ratio less than 115. As the diameter or width to thickness ratio is increased, the probability of local buckling occurring for large slenderness ratios increases. The global buckling effect of internal pressure is consistent with the Euler buckling equation for simple columns. The buckling lengths were proportional to $(L/r)^2$ and showed strong correlation.

Background

Related Investigations

A theoretical investigation of the buckling of cylindrical shells under axial compression and lateral pressure was done as early as 1932 by Flugge (Flugge, 1932). Flugge concluded that the internal pressure effects on buckling were negligible. It was found that Flugge's work was based on small-deflection theory which was later proven to be incorrect since hollow shells have a large deflection before reaching yield stress.

Large-deflection theory was then used by Von Karman and Tsien to explain the differences between theoretical and experimental results (Tsien & Karman, 1941). They concluded that experimental results were considerably lower than that predicted by theory. However, it was later shown that their work was incomplete since their theoretical model did not differ with respect to all the experiment parameters.

Lo, Crate and Schwartz then built a revised large-deflection theory using Von Karman and Tsien's method and compared that to Flugge's results. The results showed that a larger axial force was needed to induce buckling with increasing values of internal pressure, up to a limit where it remained nearly constant. The large-deflection theoretical buckling loads were comparable to the small-deflection theory when large internal pressures were applied. (Lo, Crate, & Schwartz, 1950)

In the late 1950's Harris, Suer, Skene, and Benjamin developed a procedure for the analysis of axial compressive loading and internal pressure buckling of cylindrical shells with a knowledge of the cylinder geometry only. This was done using a statistic correlation between experimental and theoretical values. (Harris, Suer, & Skene, 1957)

Around the same time, Fung and Sechler devised a design method which produced slightly conservative values for the buckling load of axial compression and internal pressure loadings on a cylindrical shell. (Fung & Sechler, 1957)

Similar work was done in the 1960s where hydrostatic pressures were considered differing from earlier investigations which looked at constant internal pressures. Dow and Peterson showed that internal hydrostatic pressures increased the buckling loads of empty elements. They ring stiffened their circular shells which resulted in a large amount of scattered data. (Dow & Peterson, 1960)

Sergev and Walton found that the instability criterion was entirely different for the cases of pressurized columns with open and closed ends. They concluded that nothing was gained in the critical buckling load by pressurizing the columns. However, it is noticed that their columns had large slenderness ratios and small diameter to thickness ratios. (Sergev & Walton, 1962)

A cylindrical shell under compression in the meridional direction can fail by overall buckling (global/Euler), local buckling or the material strength is exceeded. Various failure mechanisms of

cylindrical shells, as affected by initial geometric imperfections, boundary conditions, different cut-outs and load eccentricity, were identified by Weaver. (Weaver, 2000)

Considering the effects of imperfections, Donnell and Wan studied the effects of the initial imperfections of a cylindrical shell upon the critical buckling loads. It was found that imperfections caused buckling to occur prematurely. (Wan & Donnel, 1950)

Arbocz and Babcock studied the effect of general imperfections on the buckling of cylindrical shells and found that the correlation between the theoretical buckling loads and the experimental values was strong when considering global buckling. Complex equations were used to find a correlation to physical tests for local buckling and little correlation was found (Arbocz & Babcock, 1969)

Hutchinson, Tennyson and Muggeridge studied the effects of a local axisymmetric imperfection on the buckling behaviour of a cylindrical shell. They found that simple cut-outs or circular dimple are not as severe as compared to a sinusoidal distribution extending over the entire cylinder length. They found that very small axisymmetric dimple imperfections drastically reduce the buckling load of a circular cylindrical shell in axial compression. (Hutchinson, Tennyson, & Muggeridge, 1971)

Al-Shareef performed an investigation on the impact of holes on the buckling of rectangular hollow sections. This investigation showed that a reduction of the strength of up to 25% can be seen where hole sizes and positions are controlled by AISC (2005). (Al-Shareef, 2018)

Seifi investigated the effects of internal pressure on buckling of imperfect thin cylinders by varying the skew of the symmetric defect. This investigation found that a symmetric defect reduces the buckling load more than a skew-symmetric one. (Seifi, 2016)

Elastic Global Buckling of Columns

Columns are known as straight vertical members whose lengths are considerably greater than their cross-sectional dimensions. Columns are typically categorized by their proneness to buckling. Their most common application is to handle an axial compressive load. A “short” column is understood to deflect axially under an incremental load. The applied forces result in this shortening continuing until the column "squashes". However, if the column is “long”, axial shortening is seen only at the initial stages of incremental loading until the column becomes “unstable” and a displacement in a direction normal to the axial direction occurs.

This differential between the buckling shapes is directly related to the diameter or width to thickness ratio and the diameter or width to length ratio when studying hollow sections. If the member has high bending stiffness, its buckling resistance is high. Also, when the members length is increased, the buckling resistance is decreased.

Euler–Bernoulli's critical load equation is a simplification of the linear theory of elasticity which provides a means of calculating the load at which instability would occur. When considering the elastic behaviour of a perfect pin-roller column Euler makes the following assumptions:

- The column is perfectly straight along its entire length and the cross-sectional dimensions remain constant, thus a geometric perfection
- The material of the column is homogeneous and linearly elastic
- The axial compressive load is applied at the centroid of the cross-section with no eccentricity

As the value of the axial load increases towards P_{cr}, the column remains straight. At $P = P_{cr}$, the column enters the unstable state and will displace in the y direction.

The differential equation governing this deformation is:

$$-EI\frac{d^2y}{dx^2} = P_{cr}.y$$

The general solution to this equation is:

$$y = A_1 \cos x\sqrt{\frac{P_{cr}}{EI}} + B_1 \sin x\sqrt{\frac{P_{cr}}{EI}}$$

The constants A_1 and B_1 are found using the boundary conditions.

At $x = 0, y = 0$ which sets $A_1 = 0$. At $x = L, y = 0$ which sets

$$\sin \lambda\sqrt{\frac{P_{cr}}{EI}} = 0$$

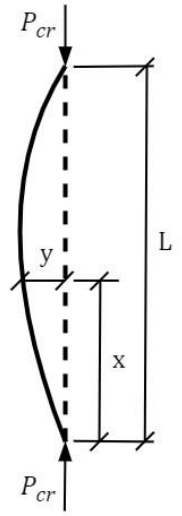

Figure 1: Simple column

This equation is satisfied when:

$$\lambda\sqrt{\frac{P_{cr}}{EI}} = 0, \pi, 2\pi, \ldots\ldots$$

$$P_{cr} = \frac{\pi^2 EI}{\lambda^2}, \frac{4\pi^2 EI}{\lambda^2} \ldots \frac{n^2\pi^2 EI}{\lambda^2}$$

The lowest value of the critical load is given by:

$$P_{cr} = \frac{\pi^2 EI}{\lambda^2}$$

Based on the initial assumptions, the Euler buckling analysis will lead to the following conclusions:

- The column will remain straight until P reaches P_{cr}
- At $P = P_{cr}$, the column will buckle in the shape of a half sine wave
- At values of $P = nP_{cr}$, other sinusoidal buckling shapes are noticed

Elastic global buckling or instability is the condition in which the element, without a tendency to return, deflects from its original position independent of the magnitude of yield stress.

In order to study the buckling nature of the models versus Euler buckling and the yield stress, it is convenient to study the onset of elastic buckling in terms of the mean applied compressive stress.

$$\sigma_{cr} = \frac{P_{cr}}{A} = \frac{\pi^2 EI}{A\lambda^2}$$

This implies that the column will fail by buckling at σ_{cr}. However, this curve is reduced to a maximum value of σ_y, where σ_y is the yield stress of steel.

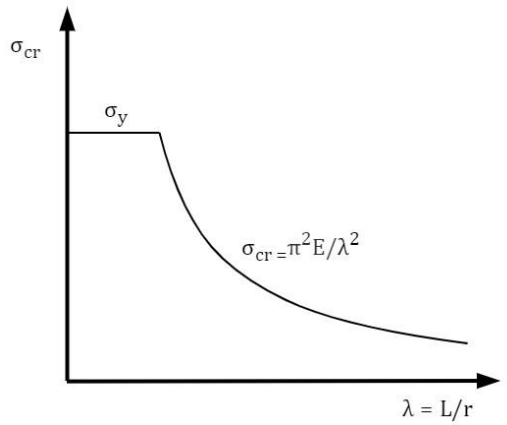

Figure 2: Graph of mean buckling stress versus slenderness ratio of a column

Structural steel has a high yield and ultimate strength when compared with other construction materials. Hence compression members made of steel tend to be relatively slender. Buckling is of interest while employing steel members, which tend to be slender, compared with reinforced concrete or prestressed concrete compression members. Members fabricated from steel plating or sheeting and subjected to compressive stresses also experience local buckling of the plate elements.

Elastic and Plastic Local Buckling of Columns

For a given cross-sectional area of a closed section, a higher moment of inertia can be achieved by increasing the diameter or width and decreasing the thickness. However, buckling of the elements of the cross-section may take place before the overall column buckling by lateral buckling or yielding. This is called local buckling. A limitation must be set on how thin-walled a closed section can be.

Research has shown that closed sections are likely to buckle in sinusoidal waves. The capacity of columns is reduced by local buckling due to a reduction in the stability of the elements which make up the cross-section. Theoretically, when steel is in its elastic state there is no strain hardening and material imperfections will not throw the elements of the section into the buckled

state. It is therefore desirable to avoid local buckling before the section yields. However, thin-walled cold-formed steel members usually experience local buckling of plate elements before the yield stress is reached.

Research has shown that reserve strength exists in plates beyond the point of elastic buckling. Utilization of this reserve may also be the objective of a more effective design. Local buckling may be allowed in some cases. This introduces the concept of plastic theory and hence the need for section classification.

This investigation studies the effects of internal pressure on local and global buckling, where all classes of sections are included.

Physical Imperfections of Hollow Sections

When studying the Euler (σ_{cr}) equation, perfect conditions are assumed. In Practice, perfect conditions are not achievable. Material and geometric imperfections obscure the results, most often reducing the strength of the element. The imperfect conditions can be summarised as:

- Loads applied eccentrically to the centroid of the element
- Initial out of straightness or rotation of the element
- Initial out of diameter/width or local impairment of the element
- Residual stresses or material impurities

This investigation considers two types of geometric imperfections. One is the initial out of straightness of the member and the other is the initial out of diameter or width. ISO 657-14 is referred by SANS 10162 for the dimensional and sectional property limits of hot-finished circular and square hollow sections. (ISO-657-14, 2000)

The percentage out-of-roundness O_r of a circular hollow section (CHS) shall be calculated from the following equation:

$$O_r = \frac{D_{max} - D_{min}}{D} \times 100\%$$

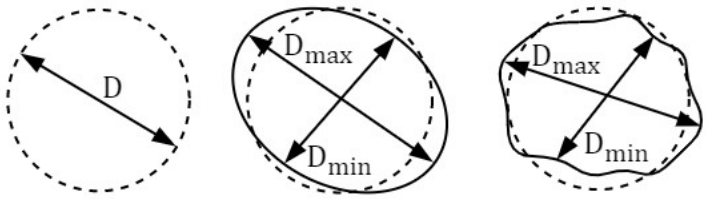

Figure 3: Schematic of out-of-roundness imperfections in CHS

For square hollow sections (SHS) the percentage concavity or convexity shall be calculated as follows:

$$\frac{x_1}{B} \times 100\%$$

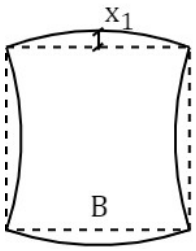

Figure 4: SHS concave and convex imperfection

The deviation from straightness e of the total length of a hollow section shall be measured at the point of maximum departure of the hollow section from the straight line connecting its two ends.

The percentage deviation from straightness is calculated as follows:

$$\frac{e}{L} \times 100\%$$

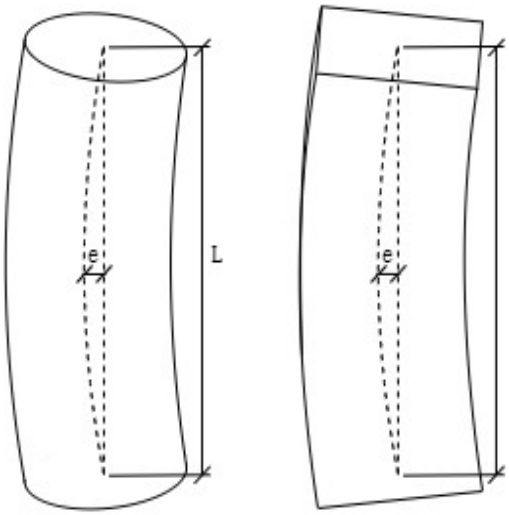

Figure 5: Out-of-straightness imperfection of CHS and SHS

EN 1993-1-6 (2007) is referred to for thin-walled elements where a local buckling mode known as elephant foot buckling is accounted for. Here, sinusoidal curves of imperfection are limited in the meridian direction with a half wavelength L_q equal to $25 \times thickness\ (t)$ of the wall and not exceeding 500mm. (1993-1-6, 2007)

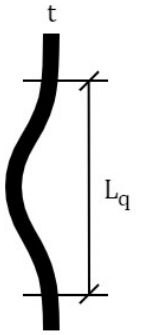

Figure 6: Elephant foot buckling half wavelength, Lq

Table 1: Table of allowable imperfections for circular and square hollow sections to ISO-657-14

Characteristic	**Circular hollow sections**	**Square hollow sections**
Outside dimension (D, B)	±1%, with a minimum of ±0.5mm and a maximum of ±10mm	±1%, with a minimum of ±0.5mm
Out-of-Roundness O	**ISO-657-14:** 2% for hollow sections having a diameter-to-thickness ratio not exceeding 100 **EN 1993-1-6:** 3% for D≤0.5m, 1.5% + 2%(1.25m-D) for 0.5m<D<1.25m and 1.5% for 1.25m≤D	-
Straightness	0.2% of the total length	0.2% of the total length
Concavity/Convexity	-	1%
Dimple Tolerance	$1.6\% \times L_q$	-

Perturbed Theoretical Equations

Contributions to the theory of imperfections in columns by Perry Robertson and Duthiel is the basis for buckling formulation in EN 1993. (F AA Crane, 1997). The theoretical lower bound curves of buckling for out of straightness members are from:

$$\sigma_m = \frac{1}{2}\left[\sigma_y + \sigma_e(1+\theta) - \sqrt{\left(\sigma_y + \sigma_e(1+\theta)\right)^2 - 4\sigma_y\sigma_e}\right]$$

- σ_m is the average longitudinal stress in the beams cross-section
- σ_y is the materials elastic limit
- $\sigma_e = \sigma_{cr}$, which is the columns Euler load

Robertson conducted an extensive series of tests to propose that θ should be taken as proportional to the slenderness ratio. He recognised that slender columns are likely to be less straight than stiff ones. This research gave a maximum value of $\theta = 0.003\frac{L}{r}$.

Duthiel found this value to be too conservative and then proposed that $\theta = 0.3\left(\frac{L}{100r}\right)^2$. (R.C. Coates, 1988).

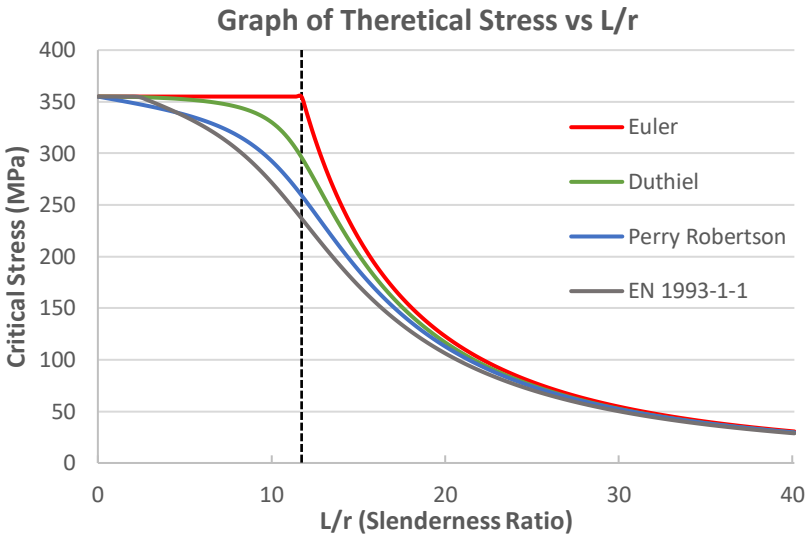

Figure 7: Typical graph of stress vs slenderness ratio for straight and curved columns under axial compression

This investigation applies the imperfections discussed and relates these results to theoretical values. The magnitude of the peak code value is used together with an increased value to maximize the effects of imperfections outside the code restrictions.

Numerical Experiment Setup

Hollow Section Geometry

To understand the full effect of internal pressure on the buckling of hollow sections, multiple parameters were varied. Since global buckling is highly susceptible in slender members, the length (L) to radius of gyration (r) ratio was increased to the extent where global buckling was noticed at stresses below the yield point (σ_y). This would ensure that the critical stress σ_{cr} curve for each L/r ratio would approach the Euler curve.

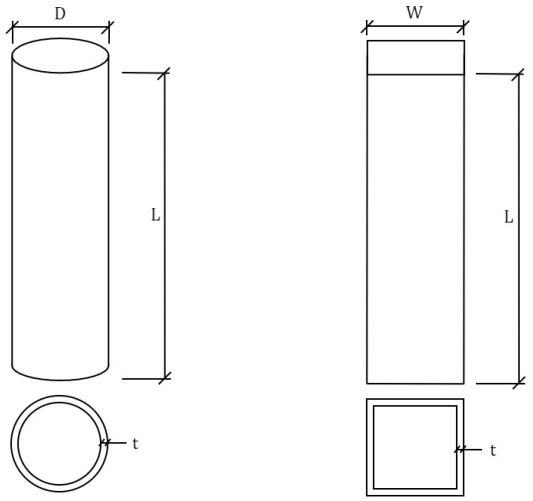

Figure 8: Dimensions for Circular and Square Hollow Sections

For thin-walled elements, local buckling is likely to govern at larger L/r ratios than thick-walled. This is dealt with in design codes using section classification. To understand the local buckling behaviour of circular hollow sections (CHS) and square hollow sections (SHS), the diameter (D) to thickness (t) and width (W) to thickness (t) ratios were varied.

The magnitude of the D/t and W/t ratios were increased to the point where local and global buckling mode shapes were found. The mode shapes were resembled, where the amplitude of imperfection was increased beyond the code limits to potentially discover new mode shapes.

Applied Loads and Boundary Conditions

Two boundary conditions for each element was investigated. The fixed roller (FR) boundary condition exemplifies the local buckling mode shapes, while the pinned roller (PR) allows for global buckling at lower slenderness (L/r) ratios.

Two load cases for each section was considered, one being an axial force only and the other being the same axial force in combination with a depth dependent hydrostatic pressure. This investigation studies how global and local buckling induced by an axial force can be affected by internal pressures.

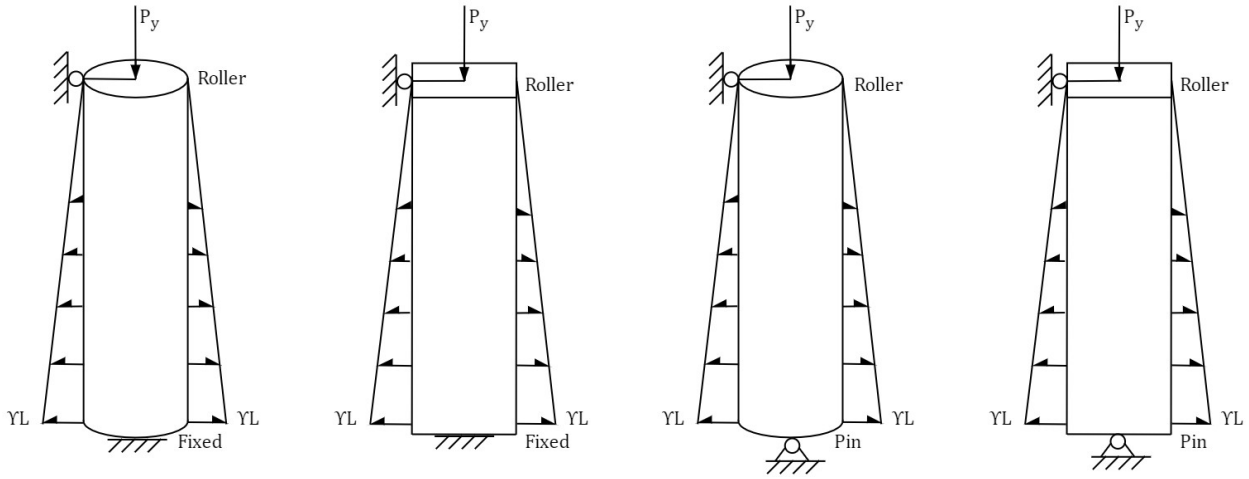

Figure 9: Diagram of loaded CHS and SHS under Fixed Roller (FR) and Pinned Roller (PR) boundary conditions

The magnitude of the applied axial force was set to be dependent on the gross area of the section. An assumption was made that the applied load would be large enough to overcome the predicted stiffness enhancing effect of the internal pressure within the first 10 buckling modes. Also, critical stress values greater than σ_y would be unreal since σ_y is the upper limit.

The applied axial force (P_y) was unique for each section, $P_y = \sigma_y \times A_g$:

- σ_y = yield stress of steel (355 MPa)
- A_g = gross sectional area of the section (m^2)

The hydrostatic pressure was applied as a function of the height where the magnitude was taken as ΥL:

- Υ = specific weight of liquid (kN/m^3)
- L = length of column (m)

Material Properties

Certain assumptions were made to correctly approximate the real-world behaviour of a material. This investigation looks at the elastic buckling nature of structural steel hollow sections.

When forces are applied to materials, some return to their original shape once the force is removed. The ability of the material to return to its original shape is called elasticity. Since this investigation focuses on the linear elastic state of steel, Hooke's law is applicable:

$\sigma = D\varepsilon$

Where:

- σ is the stress vector
- ε is the strain vector

- D is the elasticity matrix, which is a function of Young's Modulus E and Poisson's ratio ν for isotropic materials

Isotropic materials have an elasticity property that is independent of the material orientation. The material does not change its behaviour when rotated or loaded in different directions. Structural steel is modelled as an isotropic material with the following values set:

- Young's Modulus, $E = 210\ GPa$
- Poisson's ratio, $\nu = 0.3$

Finite Element Method (FEM)

The stability of columns subject to axial forces can affected by the inclusion of internal pressures. An equivalent average stress investigation would reveal a difference within design limits, which may not conclude an increase or decrease in the stability of the member. In other words, stability could improve while average stress tends towards the yield point.

It is necessary that this investigation looks at the way in which the test samples will buckle and what load factor is needed to induce this instability. In order to better understand the buckling problem mathematically, the *stress stiffening effect* needs to be applied. This effect considers that the presence of an applied load in a structure can alter the stiffness of the structure.

A tensile load will increase the lateral stiffness of an element while a compressive load will soften the lateral stiffness of the element.

When applying these principles to the eigenvalue problem, a linear buckling analysis predicts the critical load and the corresponding buckling mode shape under which the structure becomes unstable. The analysis assumes that at the critical buckling condition there exists a bifurcation point in the load-displacement curve where two infinitesimally close equilibrium states are possible. At this point, the unbuckled and buckled state exist without any change in the applied load.

The linear buckling analysis results if the deformed geometry is considered when formulating the equilibrium equations. The geometric stiffness matrix or initial stress stiffness matrix (K_G) accounts for the effective stiffness change in a structure due to the presence of internal stresses. K_G represents the effect of the geometric change on the element force vector from an existing stress state.

An initial stress matrix, $\overline{K}_G$, can be formulated from the result of a linear static analysis. In a linear buckling analysis, the stress is assumed to be proportional to the applied load and so a load factor λ with respect to the linear static analysis can be introduced, so that $K_G = \lambda \overline{K}_G$.

In a linear static analysis, the following linear equilibrium equation is solved:

$F = Ku$

Where:

- K is the global stiffness matrix
- u is the unknown nodal displacement vector
- F is the global equivalent nodal load vector

The eigenvalue problem for buckling can be obtained by considering the following homogeneous equation $(K + \lambda \overline{K}_G)\Delta u = 0$. Hence, a small displacement (Δu) occurs without any change of load applied to the structure.

This equation has a nontrivial solution if:

$|K + \lambda \overline{K}_G| = 0$

Linear buckling is represented as follows (x replaces Δu):

$Kx = -\lambda K_G x$

Where:

- λ is the buckling load factor, known as the eigenvalues
- x is a vector representing the displacement of the respective eigenvalue, also known as the buckling mode shape or eigenvector

The linear buckling solver determines what value λ needs to be such that the determinant of $K + K_G$ is equal to 0. In other words, the tangent stiffness matrix $(K + \lambda K_G)$ becomes singular. The buckling solver is used to determine what multiplication factor of the applied loads will cause the element to buckle and solves under the assumption that the structure remains linearly elastic.

In Strand7, the geometric stiffness matrix is formed based on the stress distribution of the existing static solution. In this investigation, the linear static solution is used as the initial conditions for the linear buckling solver. (Strand7, 2014)

FEM Elements

Plate elements in Strand7 (Strand7, 2014) can be used to model a column under imposed loads, with imperfections. Plate elements refer to elements whose geometry can be represented by two independent space variables defined on a plane. The material properties of structural steel can be assigned to these elements.

In Strand7, the following quadrilateral plate elements are available:

- 4-node quadrilateral elements (Quad4)
- 8-node quadrilateral elements (Quad8)
- 9-node quadrilateral elements (Quad9)

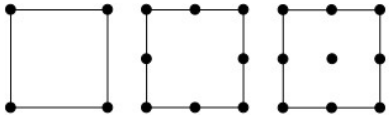

Figure 10: Quadrilateral plate element types

In order to have the best representation of results to computation, a study is performed on the quadratic element types available.

The non-linear mid-side shape functions approximate curved elements better than the Quad4 elements do. The Quad9 elements yield more accurate results than the Quad8 elements do due to the additional internal node. Each node of the 9-node plate element contains 6 degrees of freedom. That is 3 translation and 3 rotation degrees of freedom along the x, y and z axes.

Modelling Hollow Sections

The data set for this investigation was large since many parameters needed to be modified. An algorithm was prepared for both the circular and square hollow section. Nodal coordinates were programmatically set and Strand7 plate elements were connected, with their applied loads and material properties assigned. (Strand7, 2014)

A simple desktop application was built which connected to the Strand7 advanced program interface (API). The Strand7 API allows for the manipulation of geometric data, applied loads, solvers and result interpretation. The nodes were prepared, plate elements assigned, and loads applied through the API. Once the solvers had completed, the results were exported to Microsoft Excel where the graphing was automated using visual basic macros. All algorithms are described in detail. (Strand7, 2014) (Microsoft, 2019)

Figure 2 shows the usage of Quad9 plate elements as the walls of the perfect circular and square hollow sections.

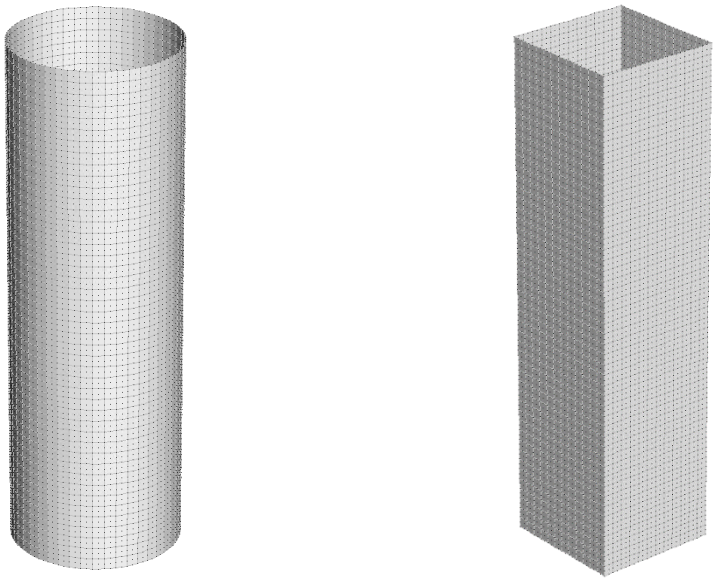

Figure 11: Perfect square and circular hollow FEM model

Modelling Imperfections

The imperfections introduced in the earlier sections are based on previous studies and code definitions. Some of these modes were seen in the buckled shapes of the perfect models. An assumption was made that the most significant effect of an initial perturbation on the buckling of the member would resemble a shape seen in the buckled mode of the perfect model.

Initial out of straightness

From previous investigations it is known that both the circular and square sections buckle globally in the shape of half sine waves. In order to induce a perturbation in this shape, the coordinates of the nodes were offset in the lateral direction of the member.

Figure 5 and Figure 12 annotates the amplitude of the sinusoidal imperfection. The algorithm used to build the perfect models was manipulated to include a term containing the relative lateral shift of the node coordinates in a single axis direction. The magnitude of this shift was determined using the following equation:

$$x = e.\sin(\pi \frac{y}{L})$$

Where e is the peak lateral position set to exceed that of the code limits.

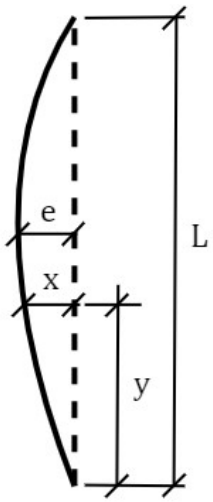

Figure 12: Annotations of out of straightness imperfection of CHS and SHS models

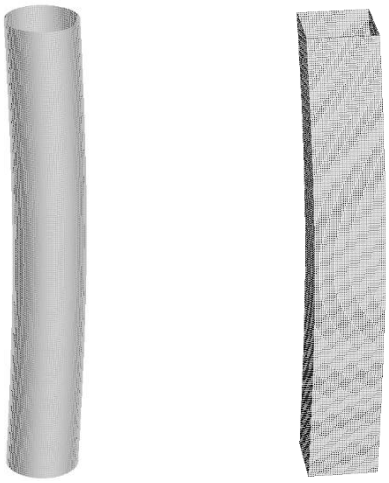

Figure 13: Out of straightness model of CHS and SHS

Initial out of width or diameter

For circular sections, Figure 3 shows the allowable imperfections along the diameter of the member as set out in the design codes. The design codes set a limitation on the magnitude of this out of diameter but do not set limitations on the its shape along the circumference or length.

In order to satisfy the assumption that a maximum effect of initial imperfection matches the mode shape, the perfect models were perturbed accordingly. When studying the local buckling mode shapes of the data set, a common nature was seen. The buckling waves of the shell of the circular section were in the form of sinusoidal waves acting along the length and circumference of the member.

An equation given by the design code to determine the out-of-diameter allowed was described in Figure 3 as:

$O_r = \frac{D_{max} - D_{min}}{D} \times 100\%$, where D is the dimeter of the circular section

The peak amplitude of the wave, e can be seen in Figure 14 and was determined as follows:

$e = \frac{O_r}{100\%} \times \frac{D}{4}$

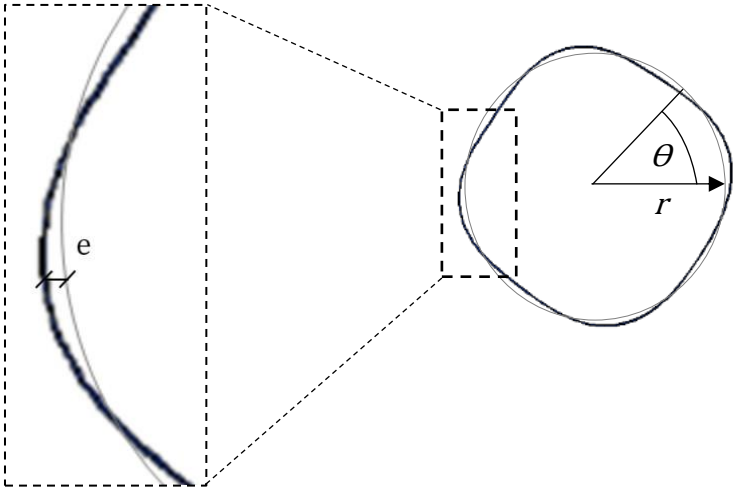

Figure 14: Peak amplitude of out of diameter sinusoidal imperfection in circular sections

To achieve this perturbed shape, the radius, r of the circular section was determine using the following equation:

$r = \frac{D}{2} + e.\sin(n\theta).\cos\left(m\frac{\pi y}{L}\right)$

$m = \frac{nL}{2D}$

Where:

- n is the number of sin waves along the circumference
- θ is the rotation angle along the circumference
- m is the number of sin waves, of similar length to the circumference waves, along the length of the element (L)

For the square sections a similar approach was taken. However, when studying the local buckling mode shapes of the perfect models, only half sine waves were noticed along the width of the member, between each wall.

$x = e.\sin\left(\frac{v\pi}{W}\right).\cos\left(m\frac{\pi y}{L}\right)$

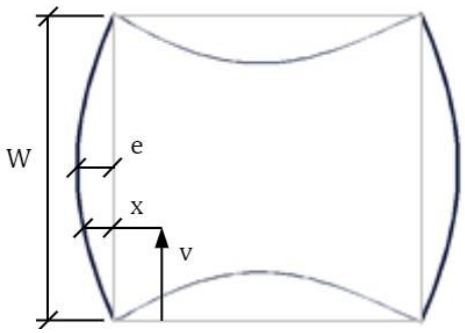

Figure 15: Peak amplitude of out of width sinusoidal imperfection in Square sections

Before compiling the final dataset and performing the experiments, a short investigation was performed for the highest diameter or width-to-thickness ratio for both the circular and square sections. The largest ratio would be the member with the slenderest elements and reveal the largest range of local buckling mode shapes. For the circular sections, this would be the member with the highest number of sine waves along the circumference.

For the square sections, all width-to-thickness ratios reveal the half sine wave as the local buckling mode. For the circular sections, 8 waves were noticed along the circumference of the section with the largest diameter to thickness ratio.

Eight sets of perturbed circular models were prepared where the number of sine waves along the circumference was the varying parameter between each experiment. All other parameters were kept constant. This investigation revealed that a perturbation with a wave count of four or six sine waves along the circumference produced the largest reduction in strength.

The following images show an exaggeration of the circular and square hollow section perturbations used in this investigation.



*Figure 16: Out of diameter CHS perturbed with **4** sine waves*

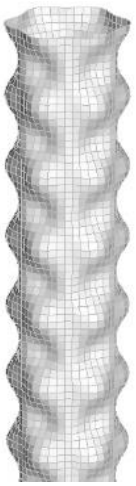

*Figure 17: Out of diameter CHS perturbed with **6** sine waves*

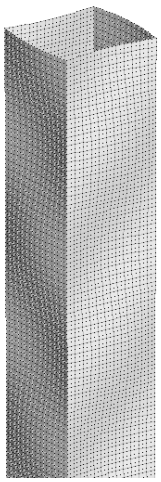

Figure 18: 0.5 Theta SHS Perturbation

Modelling Applied Loads and Boundary Conditions

When modelling a pinned or roller connection, the assumption is made that the ends of the element are bound by rigid base plates. A rigid link is used to model this condition.

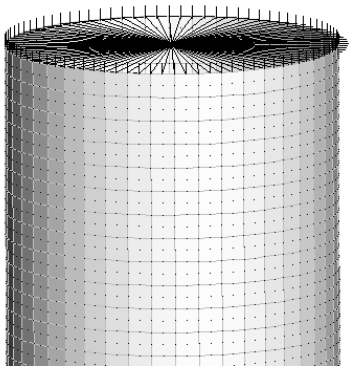

Figure 19: CHS end as rigid links

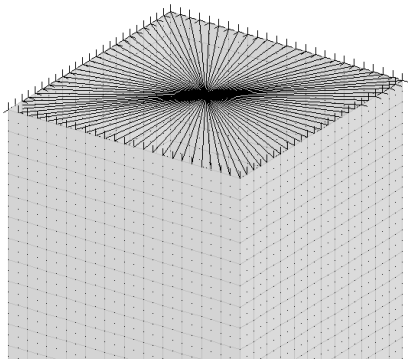

Figure 20: SHS end as rigid links

The rigid link provides restraints to the nodal rotations and displacements. It behaves as a beam member would with infinite geometric or material stiffness. Since the focus of the investigation is on the effects of local and global buckling of the section independent of connection imperfections, a rigid end plate model is needed. This ensures that unstiffened nodes at the ends of the columns do not induce premature buckling.

A reference node was created at the centre of the member. Strand7 rigid links were connected from each end node to the reference node. At this reference node, boundary conditions were set, and the axial force was applied. As shown in Figure 9 and Figure 21, normal pressures were applied to the walls of the member as a function of its length.

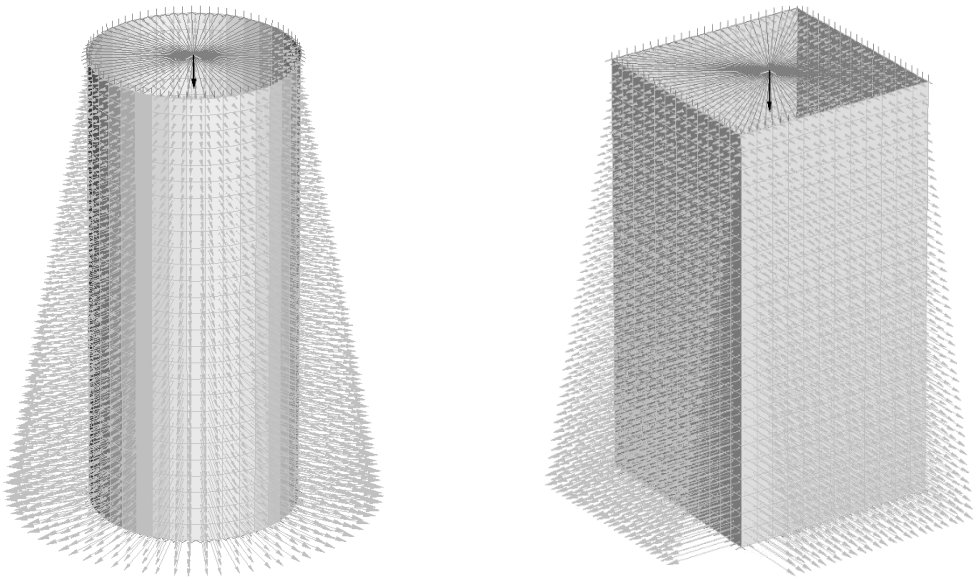

Figure 21: Finite element model of loaded circular and square hollow section

Experiment Dataset

After multiple iterations a refined dataset was prepared for the investigation. A set of width (W) or diameter(D) to thickness and length (L) to radius of gyration (r) ratios was selected. The L/r ratios were selected such that local and global buckling could be deciphered for each W/t or D/t ratio.

Table 2: Experiment dataset for Circular and Square Hollow Sections

CHS ◯			SHS □		
Diameter (mm)	Thickness (mm)	D/t	Width (mm)	Thickness (mm)	W/t
219	12	18	250	10	25
324	12	27	250	8	31
324	10	32	285	8	36
400	6	67	400	6	67
500	6	83	500	6	83
600	6	100	600	6	100
700	6	117	700	6	117
800	6	133	800	6	133
900	6	150	900	6	150

For each section type, L/r ratios ranged from 1 to 150 for both the fixed roller and pinned roller boundary conditions. Three primary model states are investigated, that being a perfect model, a globally perturbed model and a locally perturbed model. An amount of 114 square and 144 circular sections for each model state and boundary condition was tested. The dataset amounted to 684 (2 x 3 x 114) simulations of SHS's and 1152 (2 x 4 x 144) simulations of CHS's.

Convergence Study

A convergence study was performed for the circular range, where the number of divisions along the circumference was a function of the arc length. The same procedure was performed for the square sections, where the number of finite elements was a function of the width.

The lower and upper bounds of the circular and square collections were tested with a thin plate assumption in mind. The perturbed models have sinusoidal waves along the length and perimeter of the element. These models require finer meshes for accuracy.

In order to find convergence in a dataset this large, a converged finite element mesh density representing the perfect, local perturbed and global perturbed had to be tested for each boundary condition at the upper and lower extents of slenderness ratios. The finest suitable mesh would then be used for all. The suitability of the mesh density considered the computational expense allowable for completion.

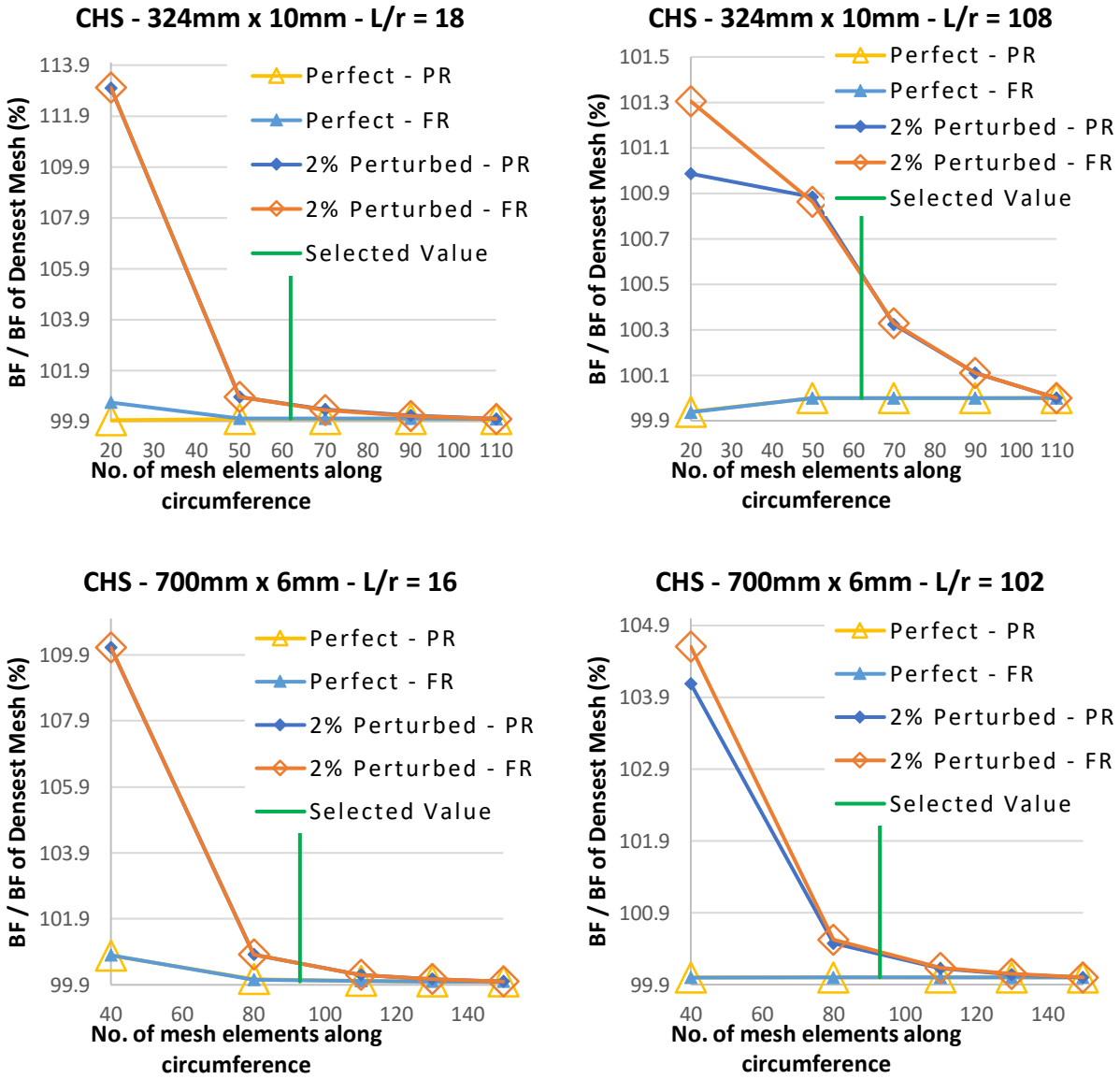

Figure 22: Convergence charts of CHS data set, for upper and lower D/t and L/r ratios

The number of divisions in the longitudinal direction was determined such that the elements aspect ratio would be as close to 1 as possible.

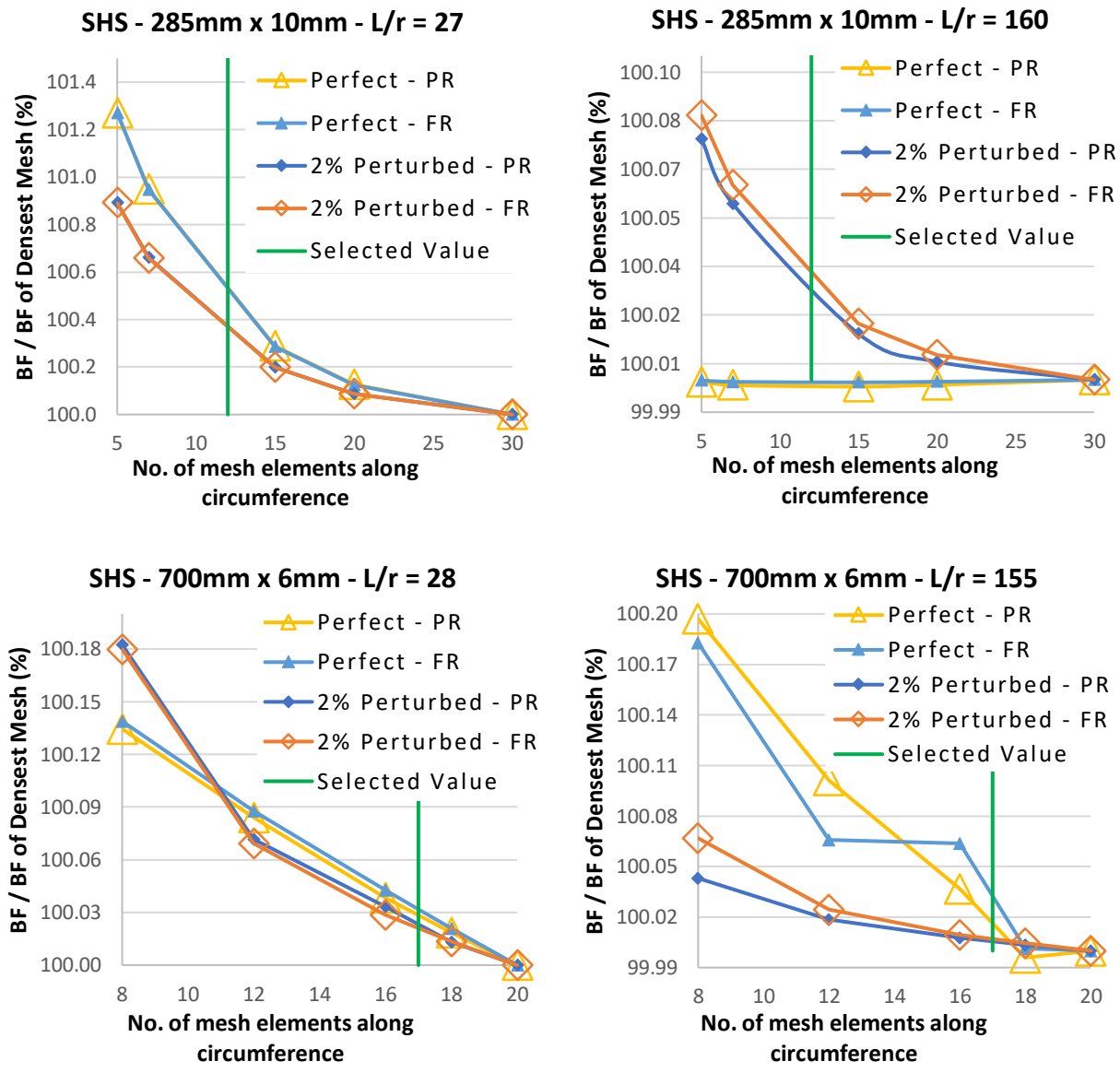

Figure 23: Convergence charts of SHS data set, for upper and lower D/t and L/r ratios

The selected number of Quad9 elements along the width or circumference of the element assumed that a difference in buckling factor (BF) between subsequently refined meshes should not alter by more or less than 1%. Therefore, the ratio of buckling factor to that of the densest mesh was limited.

The remaining datasets were linearly interpolated from the converged points. The ratio of buckling factor to that of a denser mesh was checked throughout the investigation wherever convergence was questioned. This was done by dividing each element into four and comparing the buckling factor.

Typical Converged Mesh

For a 1m long and 285mm wide SHS, 12 Quad9 elements are used across and 43 Quad9 elements used along its length. This amounts to 2064 Quad9 plate elements. Given the same length, a 700mm wide SHS has 17 Quad9 plate elements across its width and 24 Quad9 elements along its length, totalling 1632 plates and 6667 nodes.

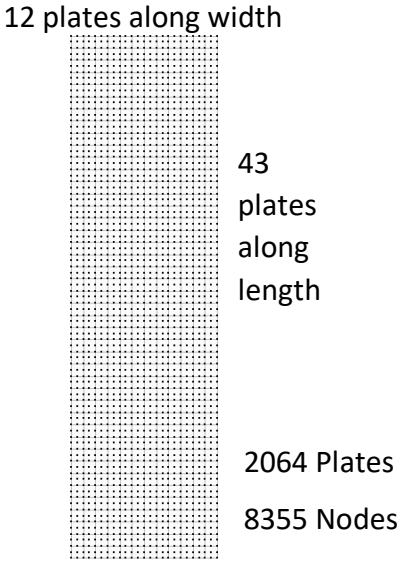

Figure 24: Converged 285mm by 1m SHS

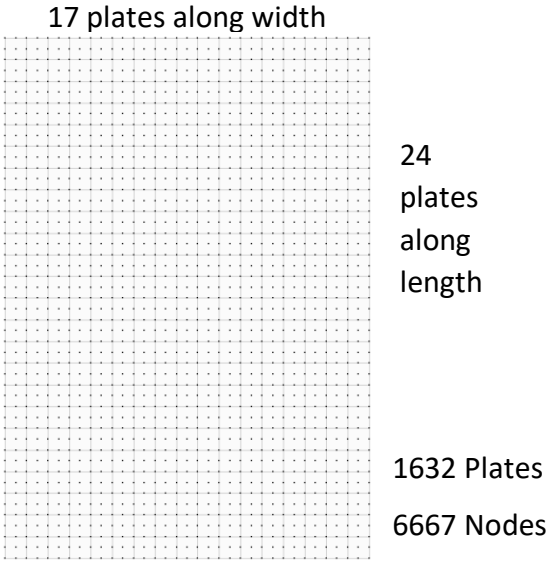

Figure 25: Converged 700mm by 1m SHS

Similarly, for CHS:

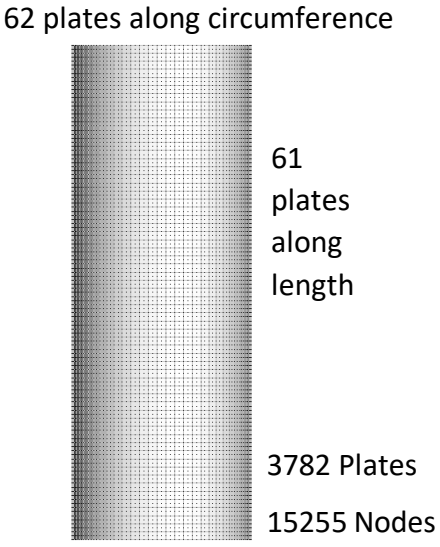

Figure 26: Converged 324mm by 1m CHS

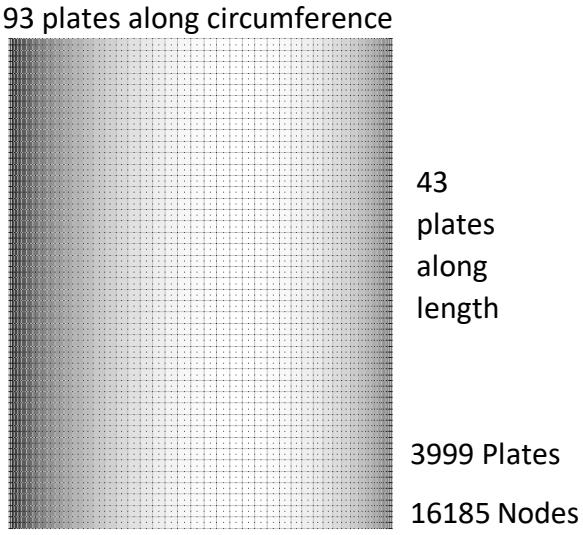

Figure 27: Converged 700mm by 1m CHS

Results

The square hollow sections (SHS) and circular hollow sections (CHS) revealed a dispersion of results according to the variance of width (W) or diameter (D) to thickness (t) ratio. Regions of local and global buckling can be seen for the pinned roller (PR) and fixed roller (FR) boundary conditions.

Circular Hollow Sections (CHS)

Perfect Models

The 219mm wide by 12mm thick (D/t = 18.25) is a class 1 section according to the Eurocode (Eurocode-3, 2005). The 324mm wide by 12mm (D/t = 27) is a class 2, the 324mm by 10mm (W/t = 32.4) is class 3. The remaining sections are class 4. All sections see local buckling in the form of sinusoidal waves along the circumference. In the state of global buckling, the Euler curve is approached.

The triangles shown in Figure 28 are typical local buckling markers for the CHS perfect models, where the 3D displacement shape can be seen in Figure 33. A detailed representation of the local buckling modes can be seen in Figure 35 and Figure 36.

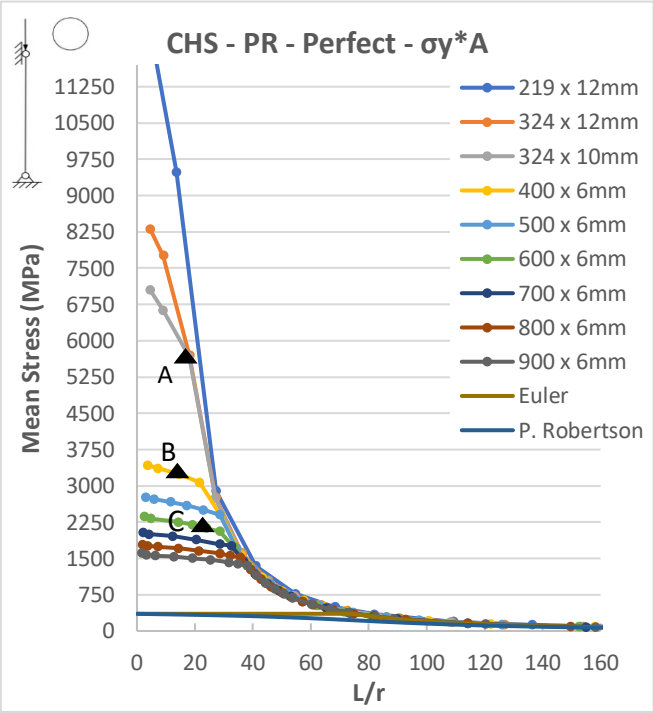

Figure 28: Perfect CHS, pinned roller with axial force only

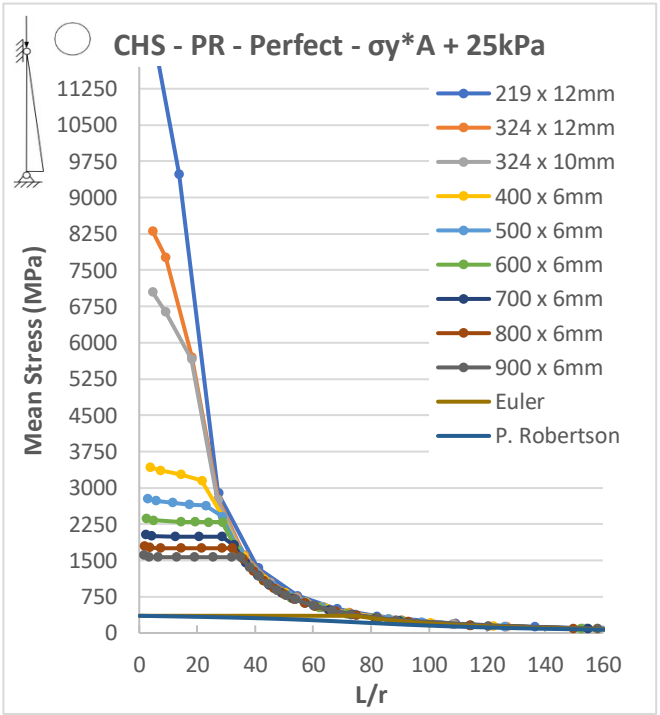

Figure 29: Perfect CHS, pinned roller with axial force & internal pressure

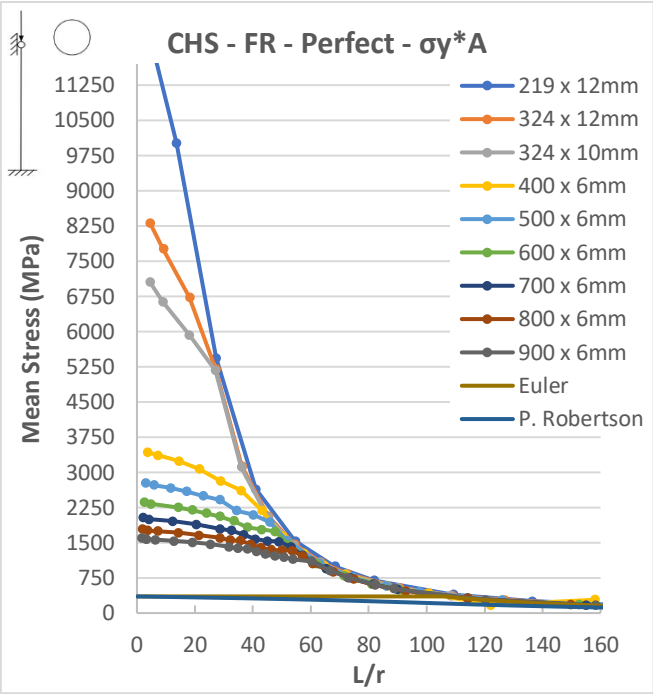

Figure 30: Perfect CHS, fixed roller with axial force only

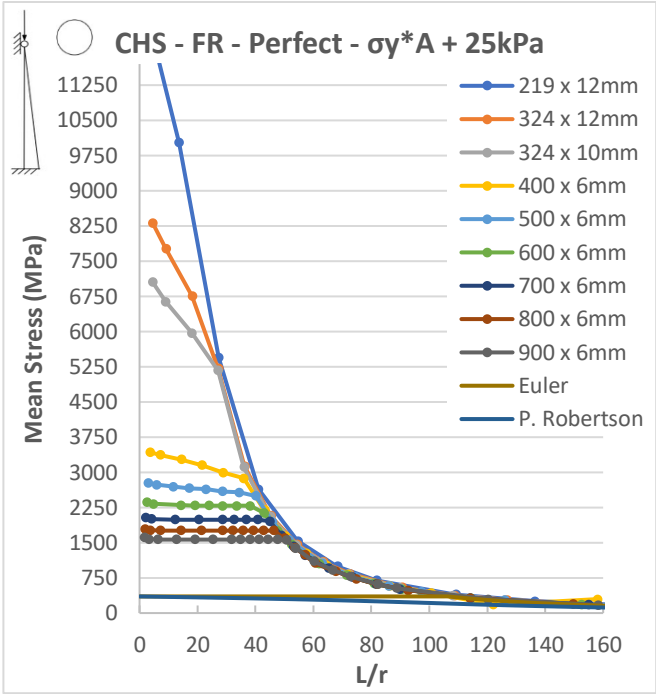

Figure 31: Perfect CHS, fixed roller with axial force & internal pressure

In all load cases and boundary conditions of the CHS perfect models, local buckling occurs at stresses higher than the yield stress of steel (355MPa).

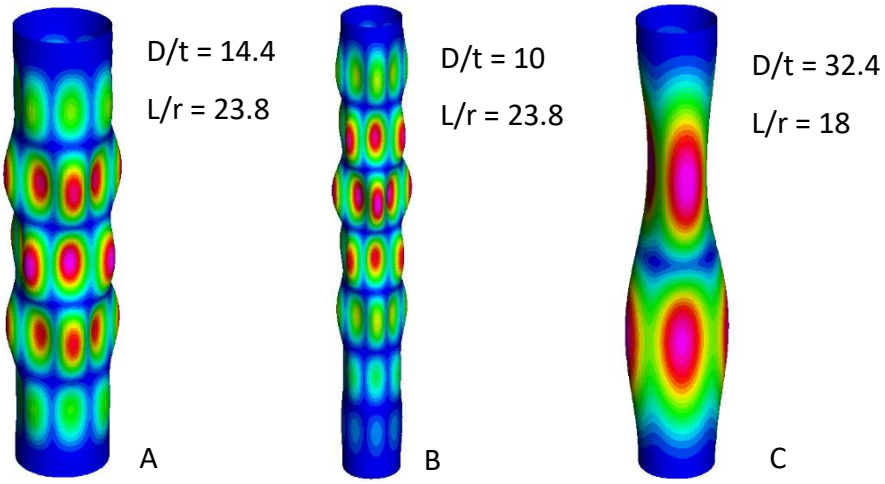

Figure 33: CHS typical local buckling mode shapes for perfect model

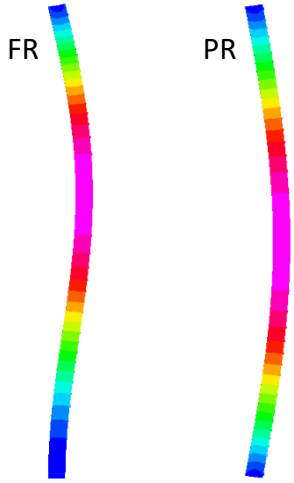

Figure 32: Typical global buckling mode shape of perfect CHS for fixed roller and pinned roller BC

Figure 35 and Figure 36 show an enlargement of the local buckling zone for the class 4 sections. This is shown for the fixed roller condition since there is a larger range of L/r ratios. In most cases, the sine wave count for the pinned roller condition matches the fixed roller condition. At increasing L/r ratios where the sine wave count reduces, the mode shape for the pinned roller boundary condition reduces before the fixed roller condition.

For both the pinned roller and the fixed roller boundary conditions, local buckling reveals an order of sine waves along the circumference that reduces with increasing L/r ratios. The values below represent the number of sine waves seen along the perimeter of the element in the buckled shape.

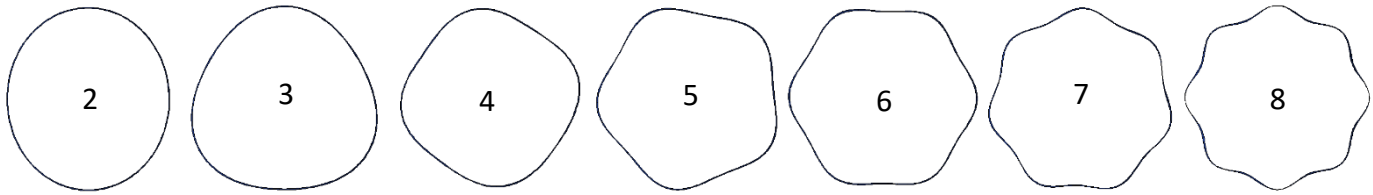

Figure 34: CHS local buckling mode shapes. Numbers represent the number of sine waves seen along the circumference.

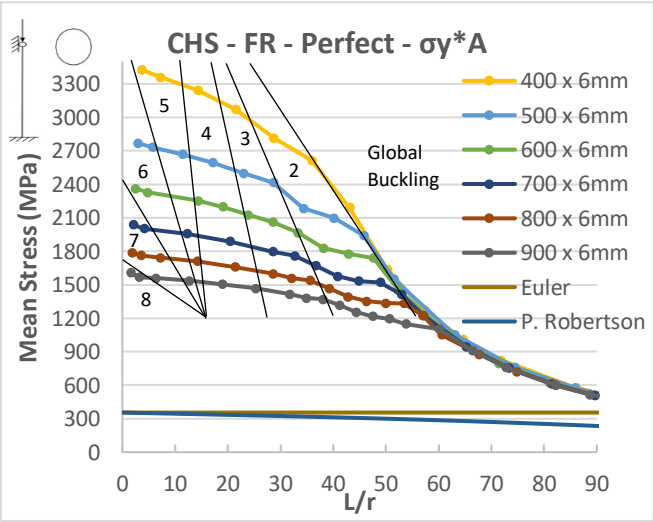

Figure 35: Local Buckling zone with sine wave count of perfect CHS, fixed roller with axial force only

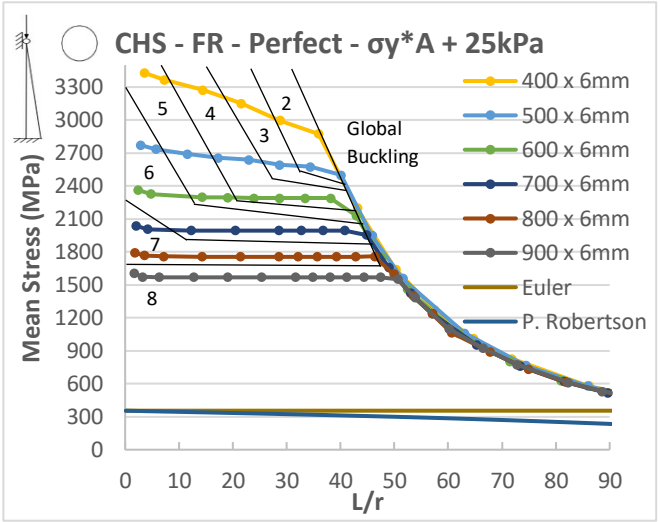

Figure 36: Local Buckling zone with sine wave count of perfect CHS, fixed roller with axial force & internal pressure

Out of Straightness (OOS)

In order to induce buckling at lower stresses, an out of straightness perturbation is introduced to the same perfect CHS range. The magnitude of the out of straightness amplitude (e) was calculated as explained in Figure 5 and Figure 15, where $\frac{e}{L} \times 100\%$ was set to 0.3%. This was set to be outside the code limits as given in Table 1.

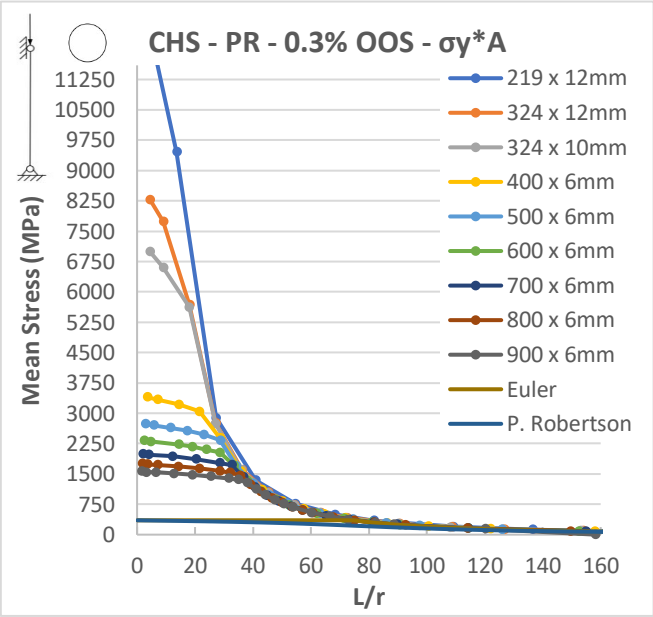

Figure 37: 0.3% out of straightness CHS, pinned roller with axial force only

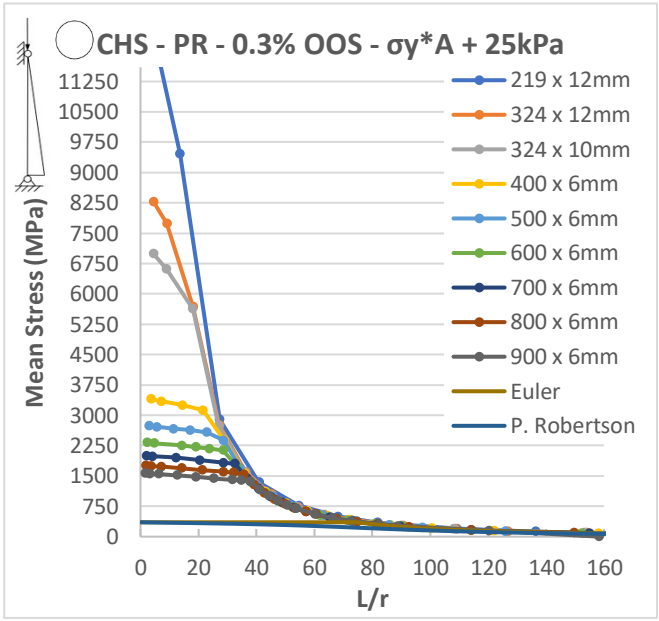

Figure 38: 0.3% out of straightness CHS, pinned roller with axial force & internal pressure

For D/t ratios less than 83, a peak drop in strength of 1% was found when compared to the perfect models. Strength reductions of 6% to 12% were seen for D/t ratios ranging from 100 to 150. This was consistent for both boundary conditions.

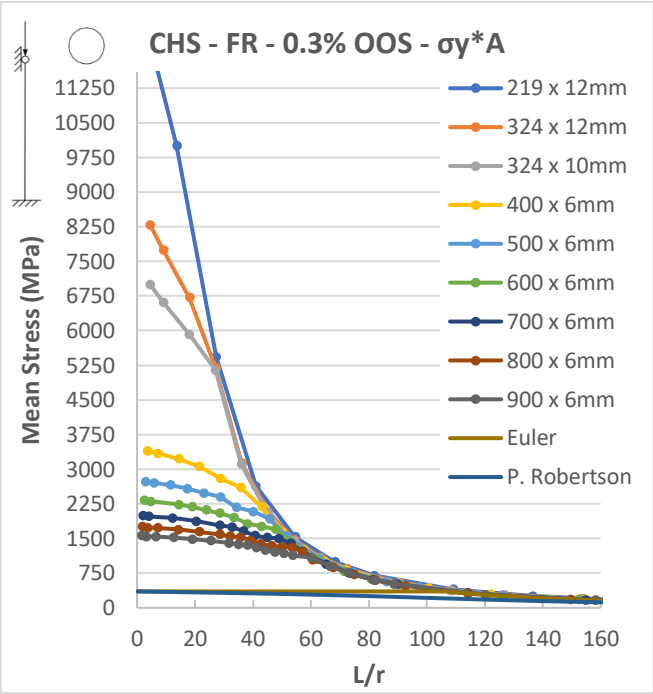

Figure 39: 0.3% out of straightness CHS, FR with axial force only

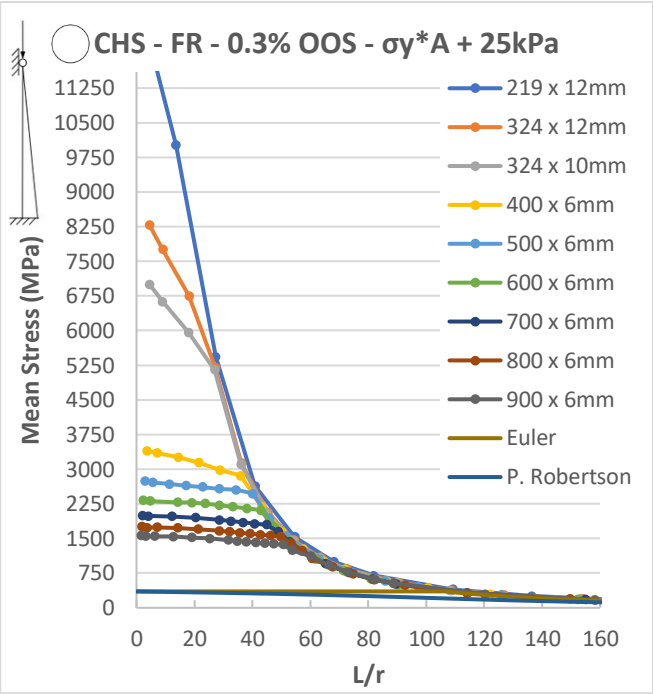

Figure 40: 0.3% out of straightness CHS, FR with axial force & internal pressure

Figure 41 below shows the mean buckling stresses for the axial only load case for class 4 sections. The strength of the member is reduced in all D/t and L/r ratios when compared to the perfect model. However, the sine wave count of each local buckling mode remains the same as the perfect models.

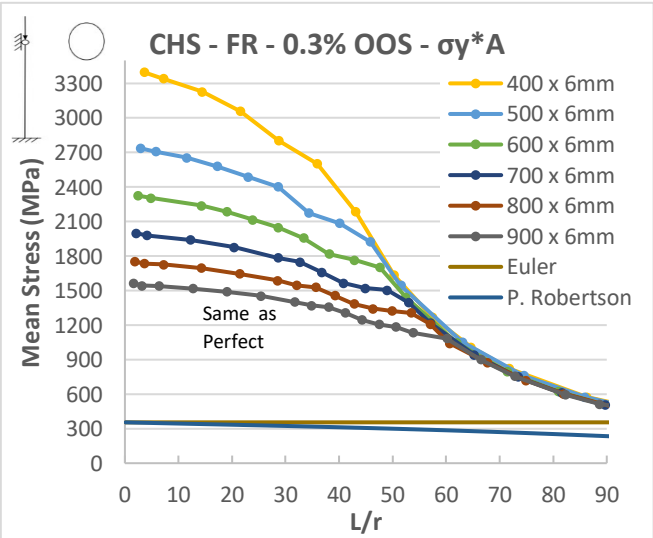

Figure 41: Local Buckling with sine wave count of out of straightness CHS, fixed roller with axial force only

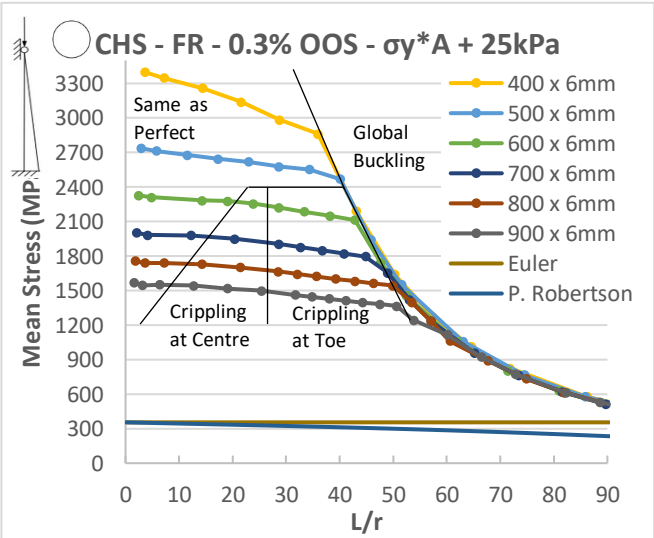

Figure 42: Local Buckling with sine wave count and crippling zones of out of straightness CHS, fixed roller with axial force & internal pressure

Figure 42 shows a new buckling mode shape that is found when internal pressures are included to curved circular hollow sections. The face of the perturbed CHS on the shorter length reveals a crippled shape. These are short waves that propel at the centre to upper half for D/t ratios greater than 100 and L/r ratios less than 27. For the same range of D/t ratios, when L/r is greater than 27 the crippling mode occurs at the toe of the element. It was noticed that the toe crippling mode was only present in the fixed roller boundary condition.

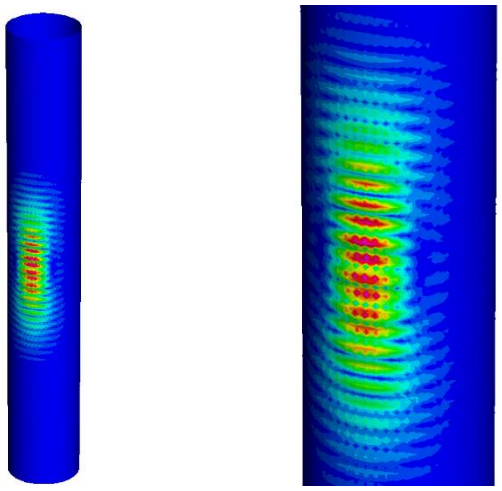

Figure 43: Crippling of shorter side of out of straightness CHS, at centre of member

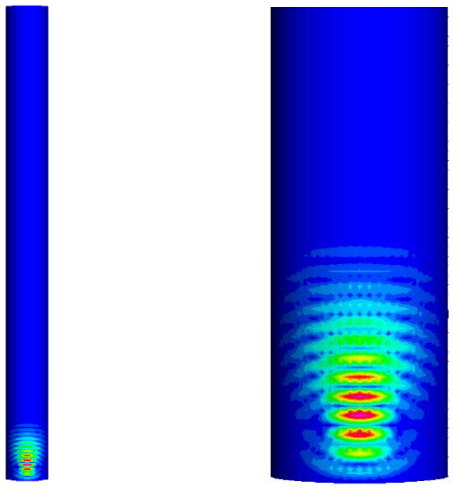

Figure 44: Crippling of shorter side of out of straightness CHS, at toe of member with fixed roller boundary condition only

Out of Diameter (OOD)

In Figure 3 the out of diameter perturbation is described where the value of $O_r = \frac{D_{max}-D_{min}}{D} \times 100\%$ is set to 3%. This was set to be outside the code limits as given in Table 1. As described earlier, the deformation shape or count of sine waves was modified in a short investigation for D/t equal to 150. The investigation looked at initial sine wave counts of 2 to 8 waves where 4 and 6 waves revealed the highest decrease in strength of the CHS. This was true for all values of D/t.

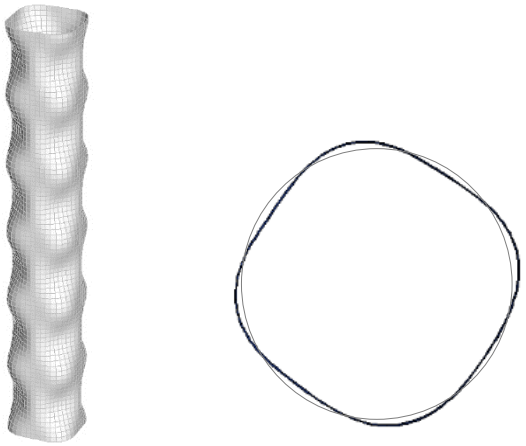

*Figure 45: Out of diameter CHS perturbed with **4** sine waves*

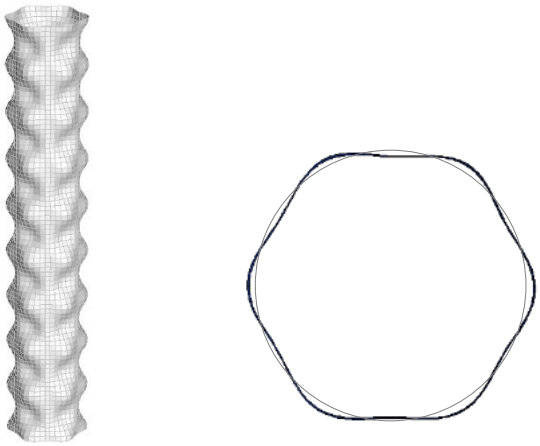

*Figure 46: Out of diameter CHS perturbed with **6** sine waves*

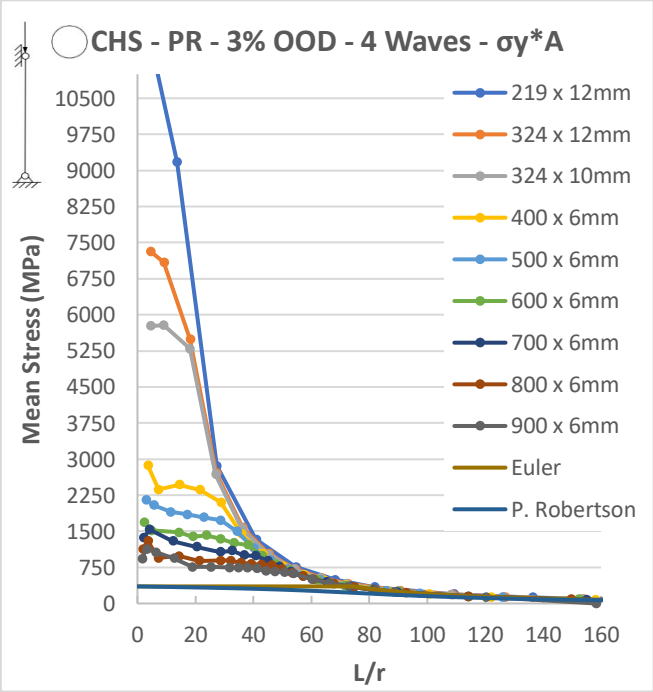

Figure 47: 3% out of diameter CHS, 4 sine waves, pinned roller with axial force only

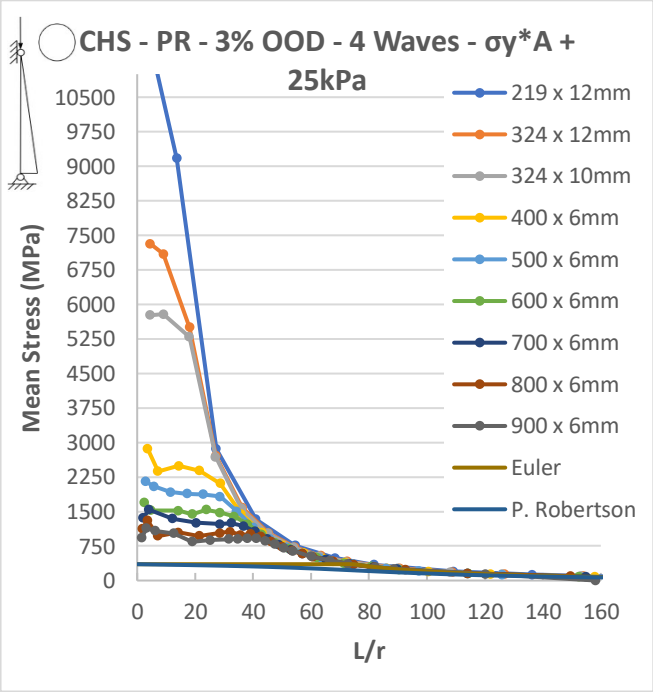

Figure 48: 3% out of diameter CHS, 4 sine waves, pinned roller with axial force & internal pressure

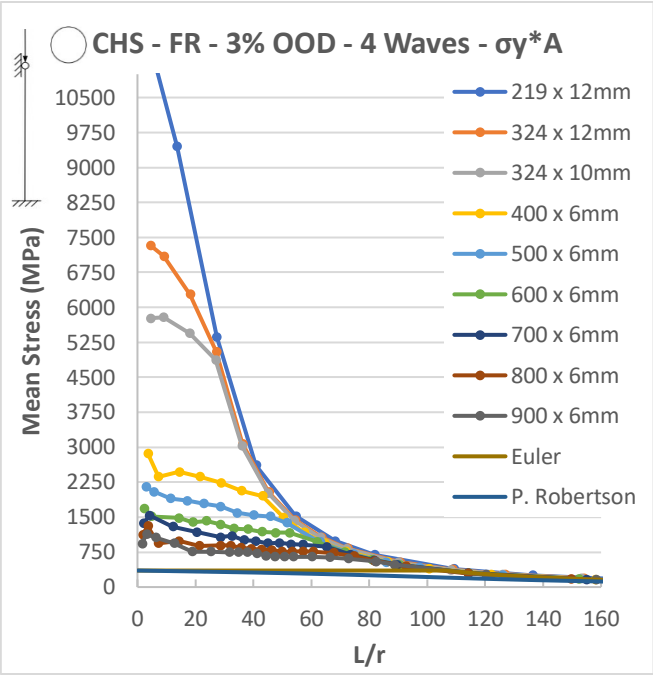

Figure 49: 3% out of diameter CHS, 4 sine waves, fixed roller with axial force only

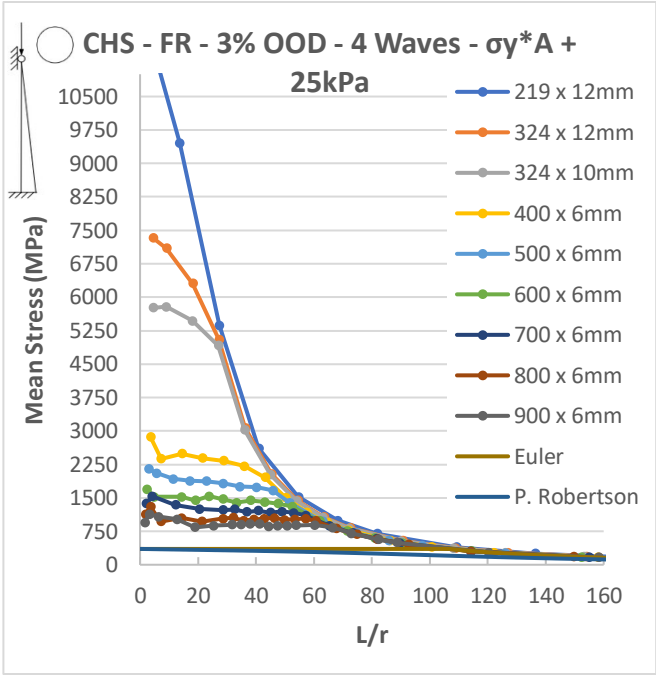

Figure 50: 3% out of diameter CHS, 4 sine waves, fixed roller with axial force & internal pressure

Figure 47 to Figure 50 show the average buckling stress for a CHS where four sine waves are introduced along the circumference of the member. This is performed programmatically by taking the value of $(D_{max} - D_{\min})/2$ when setting $O_r = 3\%$ and making it a product of $\sin 4\theta$. The diameter of the CHS is then added to this product as theta ranges from 0 to 2π. A similar procedure is done for the six sine waves where $\sin 6\theta$ is used instead.

These circumferential wavelengths are then used to determine the integer number of waves along the length of the element, whereby the modified diameter is made a product of the cosine of this integer value and theta.

A strength reduction due to the perturbation by four and six sine waves was noticed for all simulations. For four sine waves, the peak strength reduction percentage ranged linearly from 5.7% for class 1 sections to 18.3% for class 3 sections. No influence from boundary conditions or internal pressure was noticed.

For class 4 sections, the peak strength reduction percentage ranged linearly from 29.7% at D/t = 67 to 49.6% at D/t = 150. The change in boundary condition or inclusion of internal pressure made a difference of up to 1% which was deemed negligible.

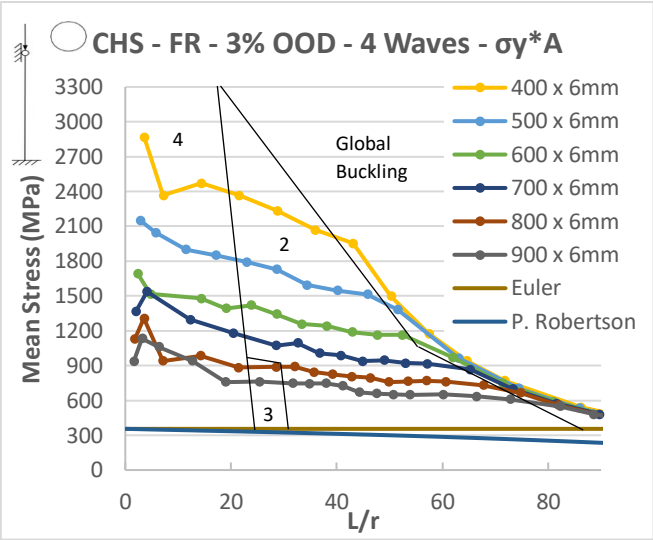

Figure 51: Local Buckling sine wave count of CHS 3% out of diameter with 4 sine waves, fixed roller and axial force only

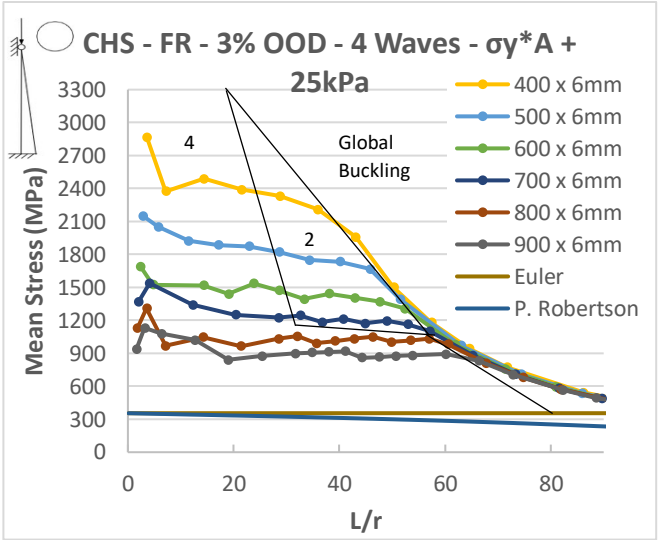

Figure 52: Local Buckling sine wave count of CHS 3% out of diameter with 4 sine waves, fixed roller, axial force and internal pressure

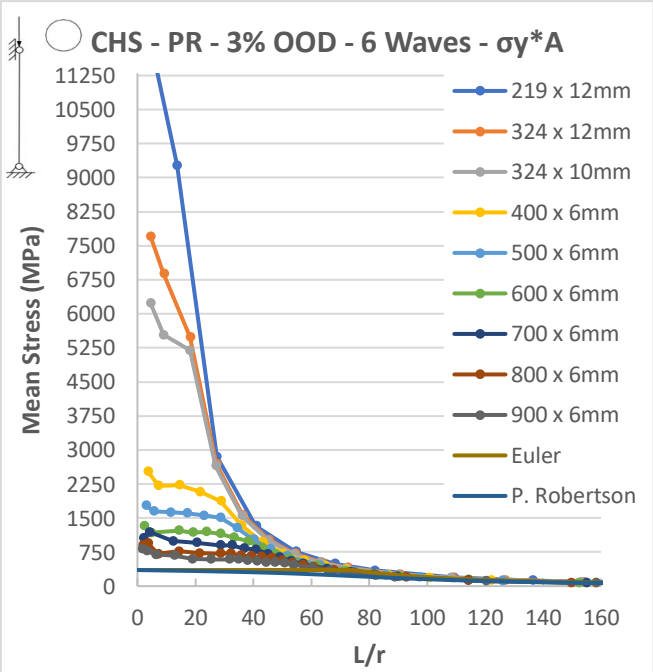

Figure 53: 3% out of diameter CHS, 6 sine waves, pinned roller with axial force only

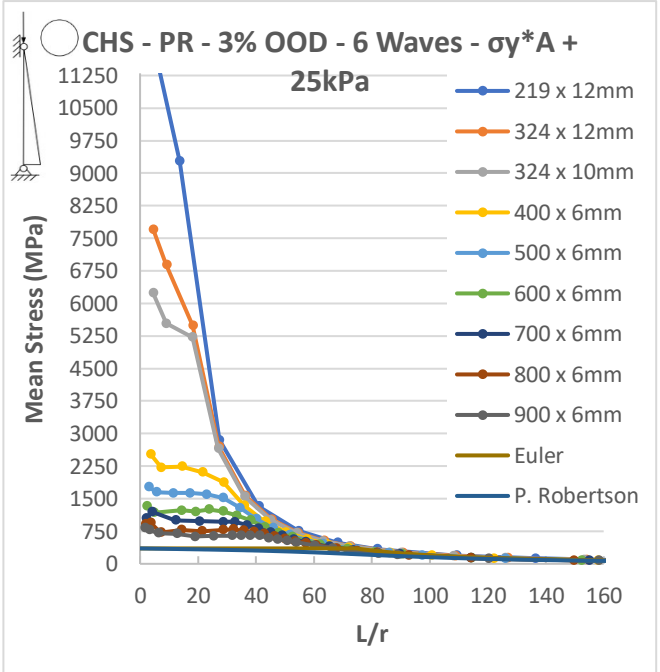

Figure 54: 3% out of diameter CHS, 6 sine waves, pinned roller with axial force & internal pressure

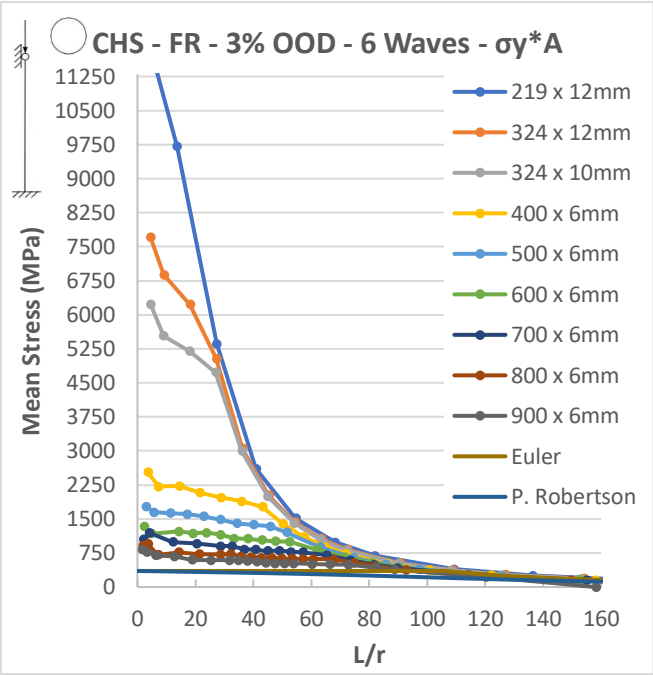

Figure 55: 3% out of diameter CHS, 6 sine waves, fixed roller with axial force only

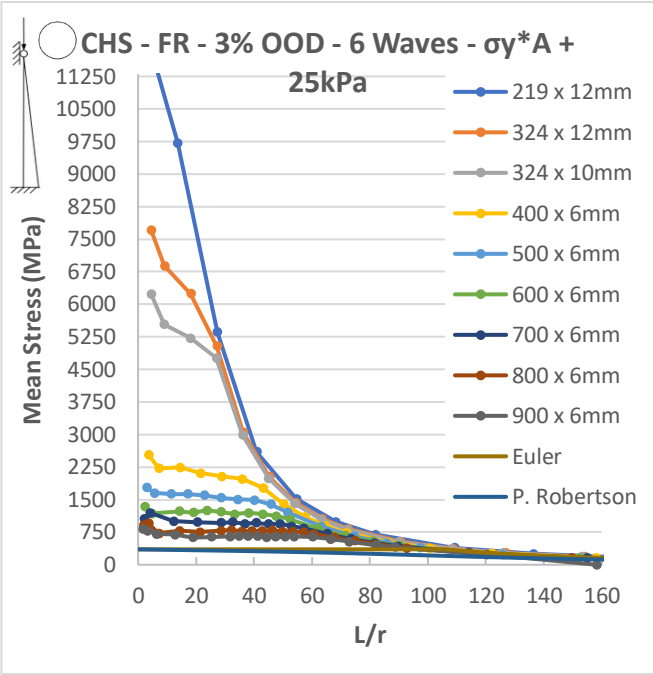

Figure 56: 3% out of diameter CHS, 6 sine waves, fixed roller with axial force & internal pressure

For six sine waves, the peak strength reduction percentage ranged linearly from 3.3% for class 1 sections to 16.6% for class 3 sections. No influence from boundary conditions or internal pressure was noticed.

For class 4 sections, the peak strength reduction percentage ranged linearly from 34% at D/t = 67 to 60% at D/t = 150. The change in boundary condition or inclusion of internal pressure made a difference of up to 1% which was deemed negligible.

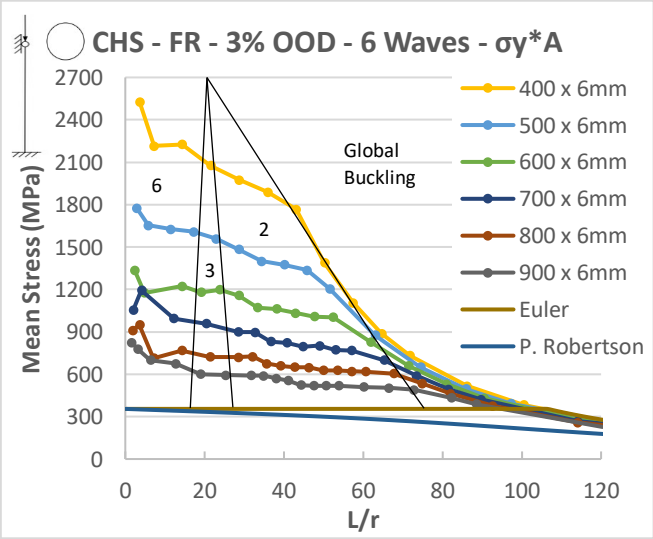

Figure 57: 3% out of diameter CHS, 6 sine waves, fixed roller with axial force only

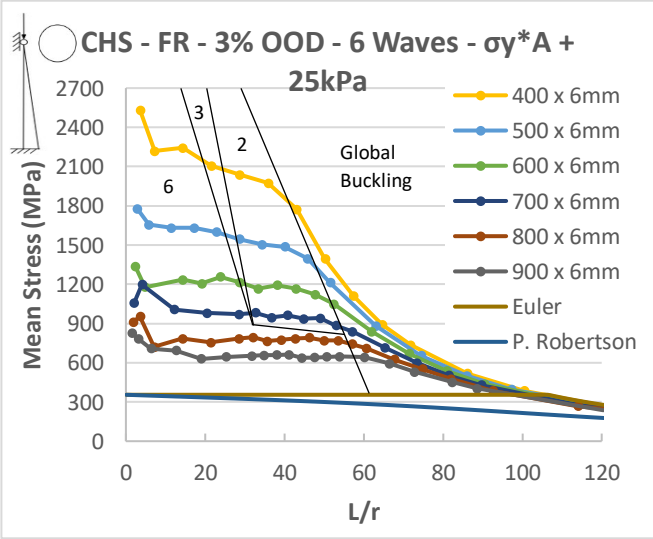

Figure 58: 3% out of diameter CHS, 6 sine waves, fixed roller with axial force & internal pressure

Square Hollow Section (SHS)

Perfect Models

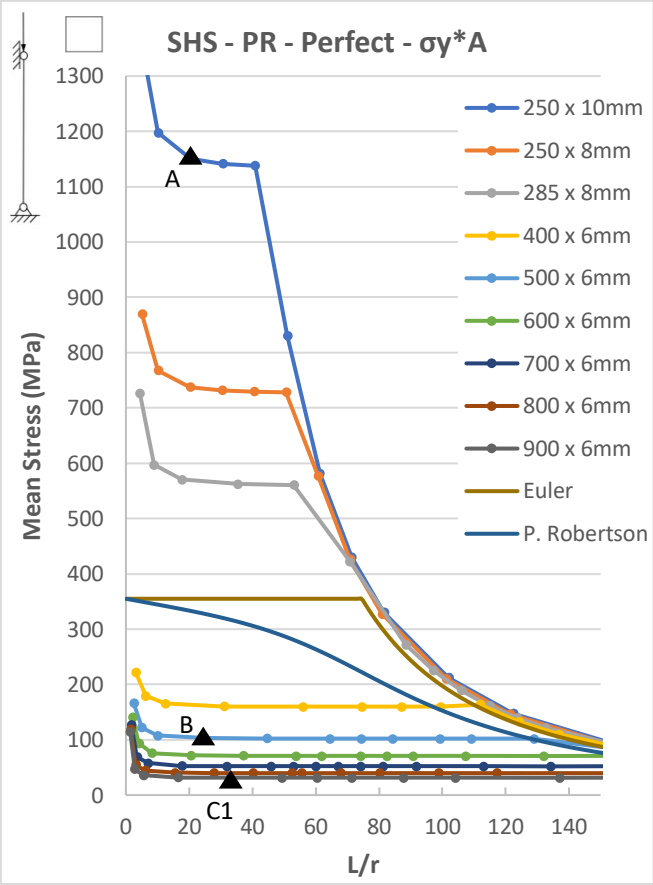

Figure 59: Perfect SHS, pinned roller with axial force only

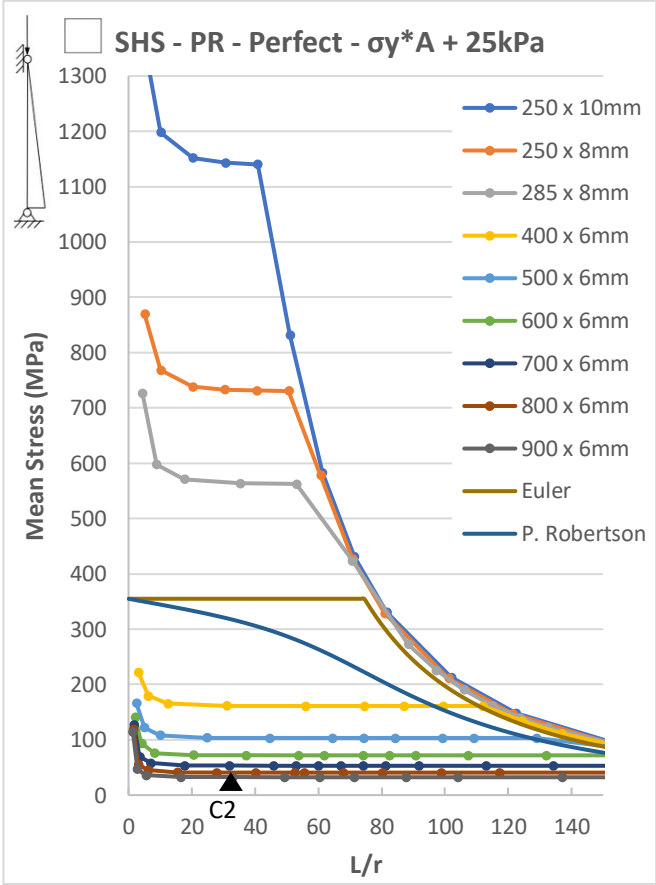

Figure 60: Perfect SHS, pinned roller with axial force and internal pressure

The 250mm wide by 10mm thick (W/t = 25) is a class 1 section according to the Eurocode (Eurocode-3, 2005). The 250mm wide by 8mm (W/t = 31.3) is a class 2, the 285mm by 8mm (W/t = 35.6) is class 3. The remaining sections are class 4.

The class 4 sections revealed local buckling below the yield stress of steel (355 JR at 355MPa). Given the L/r ratios, global buckling was not attained for the higher W/t ratio sections.

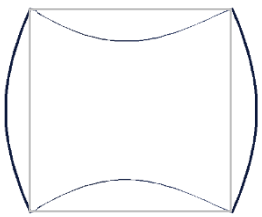

Figure 61: Cross-section of typical locally buckled SHS

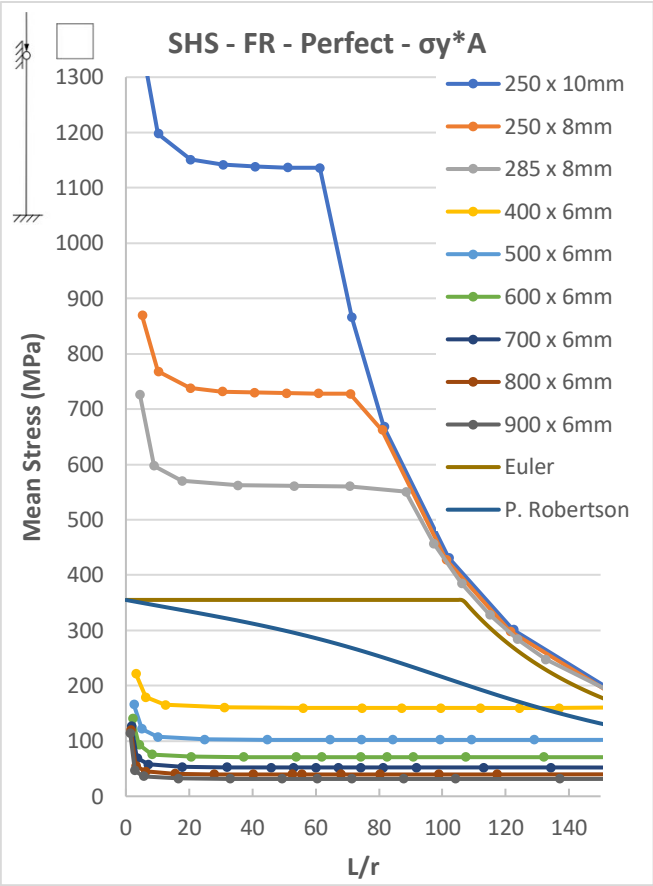

Figure 62: Perfect SHS, fixed roller with axial force only

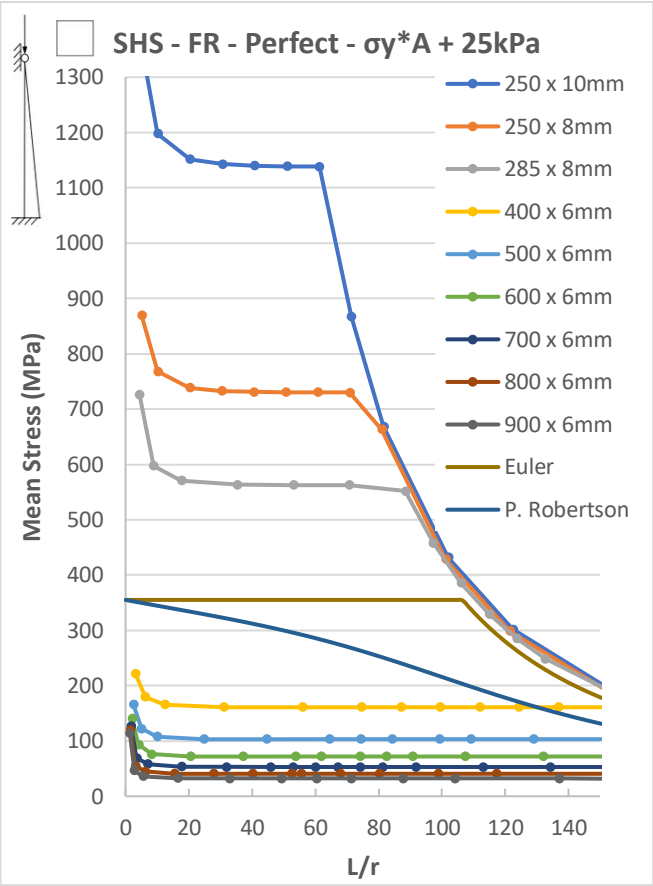

Figure 63: Perfect SHS, fixed roller with axial force and internal pressure

Both the pinned roller and fixed roller reveal the same local buckling mode for each section. This mode is the alternating concave and convex half-sine wave along the width and length of the element:

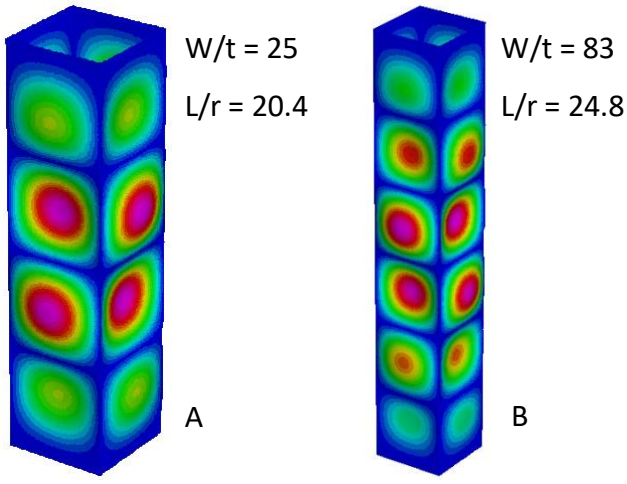

Figure 64: Typical Local buckling mode shapes of perfect SHS for various W/t and L/W ratios

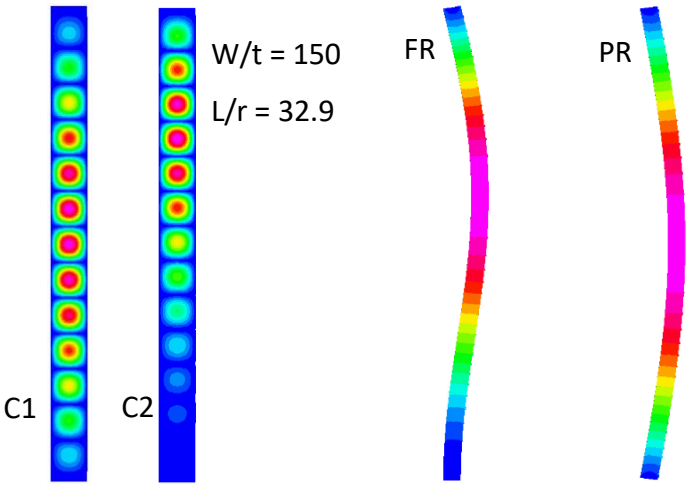

Figure 65: Typical global buckling mode shape of perfect SHS for fixed roller and pinned roller

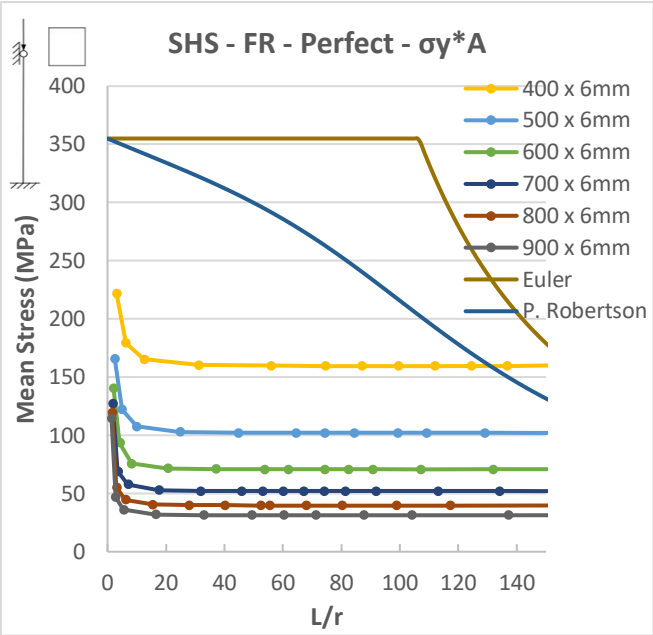

Figure 66: Local Buckling of perfect SHS, FR axial force only

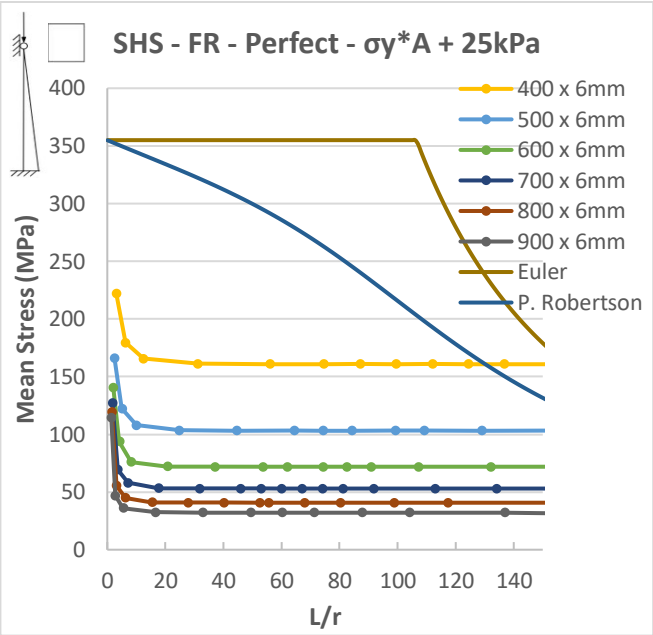

Figure 67: Local Buckling of perfect SHS, FR axial force & internal pressure

Out of Straightness (OOS)

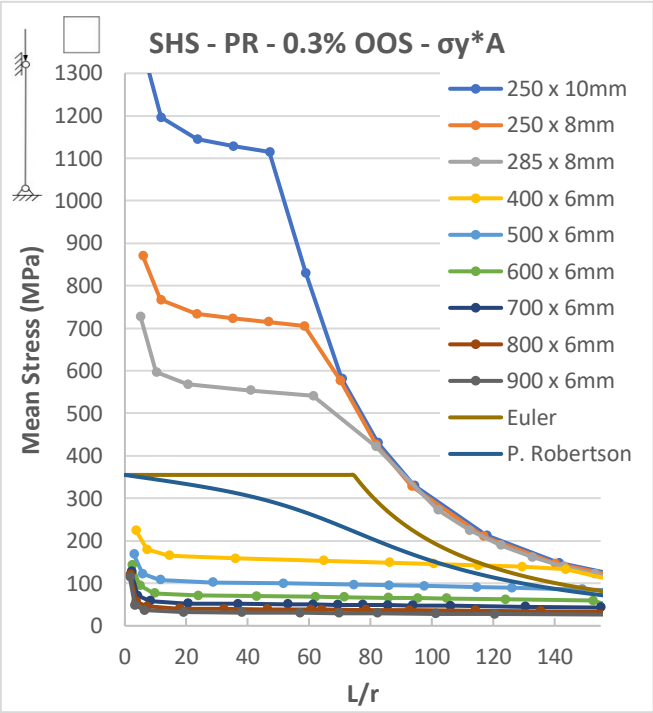

Figure 68: 0.3% out of straightness SHS, pinned roller with axial force only

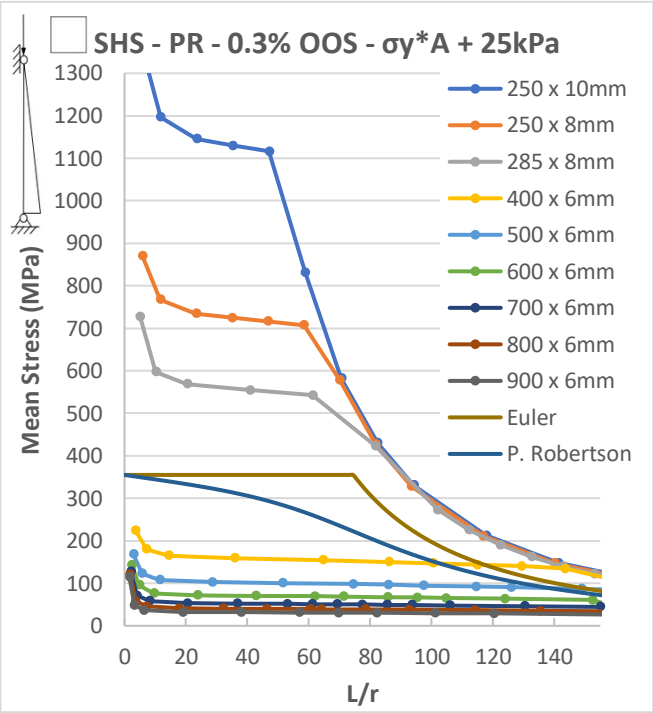

Figure 69: 0.3% out of straightness SHS, pinned roller with axial force & internal pressure

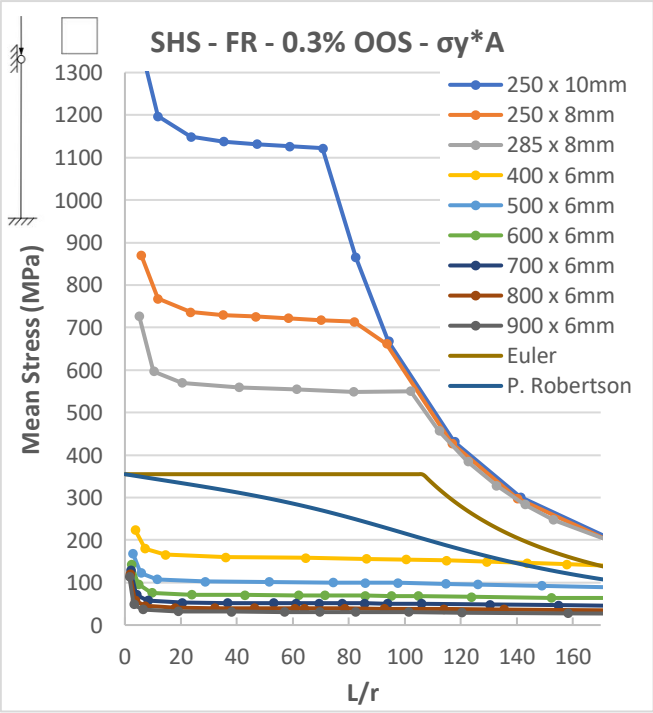

Figure 70: 0.3% out of straightness SHS, FR with axial force only

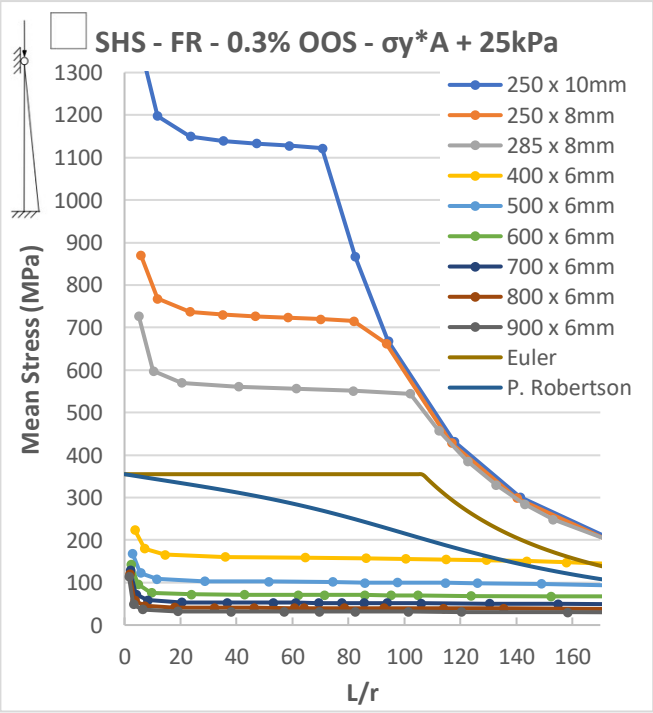

Figure 71: 0.3% out of straightness SHS, FR with axial force & internal pressure

The out of straightness perturbation produces no new local buckling modes. All match the perfect models, with the difference being that the amplitude of the half-sine wave is greater on the shorter face of the member. The internal pressure reveals a shift in the local buckling mode to the zone of lower internal pressure.

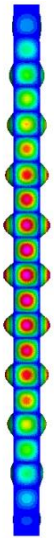

Figure 72: Local buckling of typical perfect SHS with axial force only

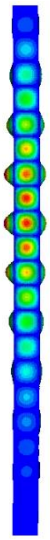

Figure 73: Local buckling of typical out of straightness SHS, with axial force & internal pressure

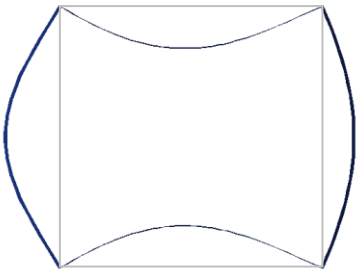

Figure 74: Cross-section of typical out of straightness SHS showing a higher amplitude on the shorter face of the member

All mean buckling stresses are higher than those seen in the perfect models, with the global buckling curve showing higher values than the Euler curve for both boundary conditions.

Out of Width (OOW)

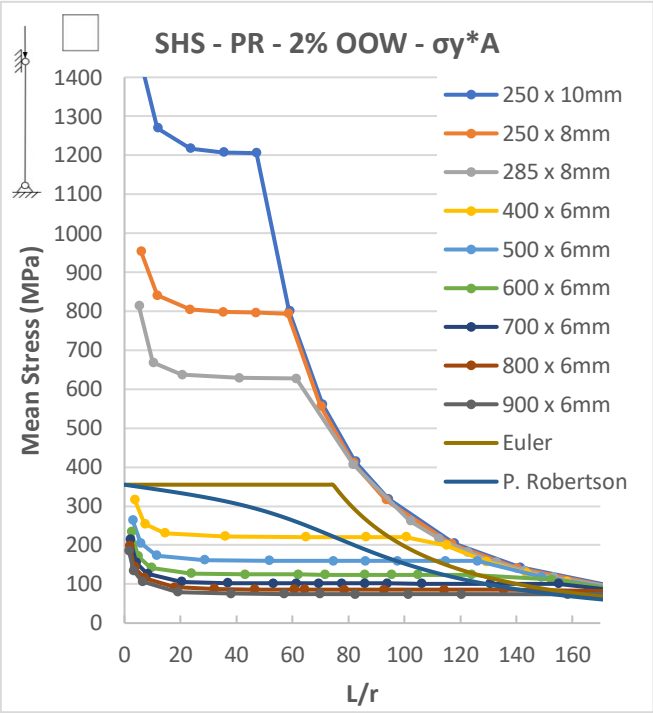

Figure 75: 2% out of width SHS, PR with axial force only

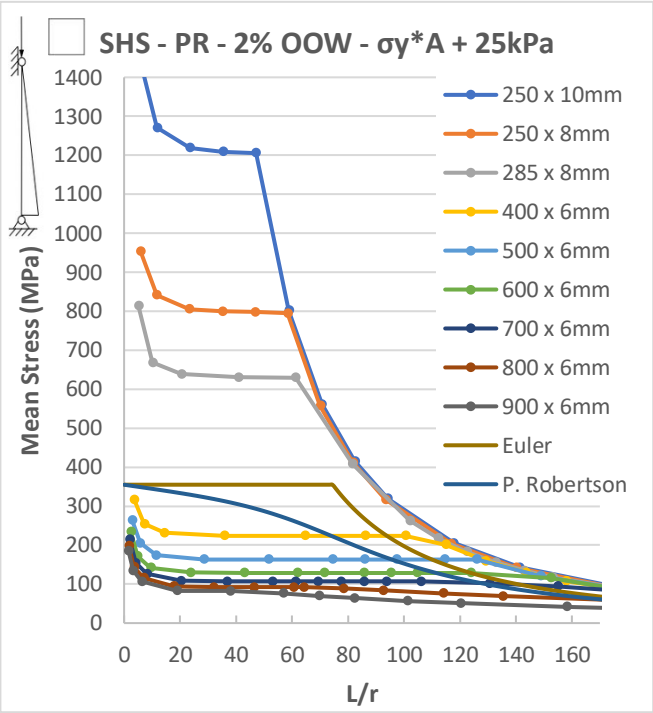

Figure 76: 2% out of width SHS, PR with axial force & internal pressure

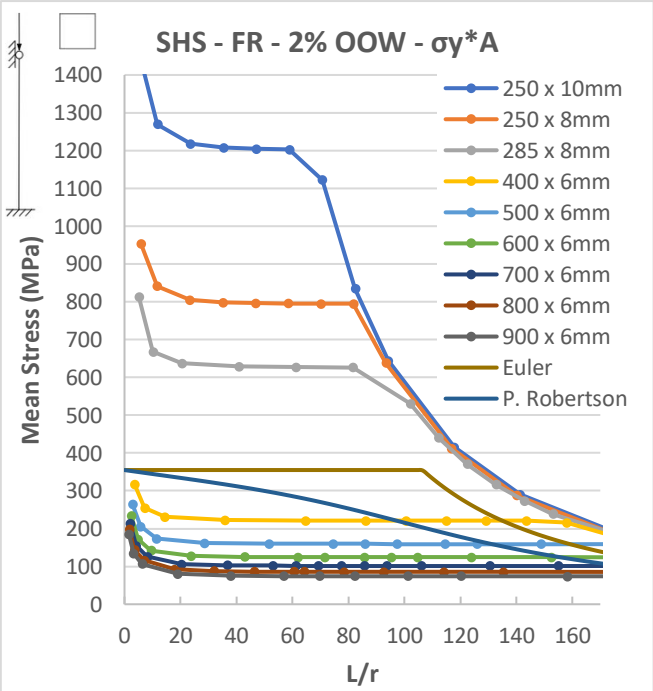

Figure 77: 2% out of width SHS, FR with axial force only

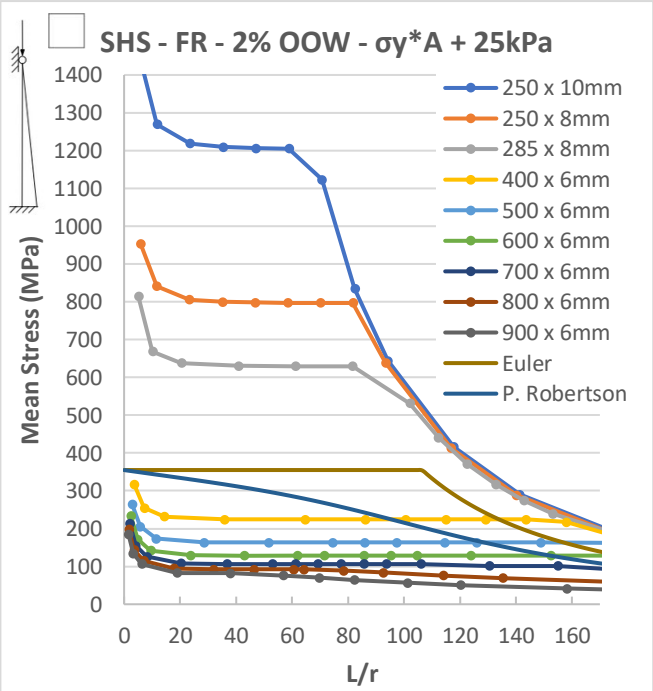

Figure 78: 2% out of width SHS, FR with axial force & internal pressure

The concave and convex width perturbation showed local and global buckling stresses greater than that of the out of straightness condition. A weak zone was noticed at the toe of the member.

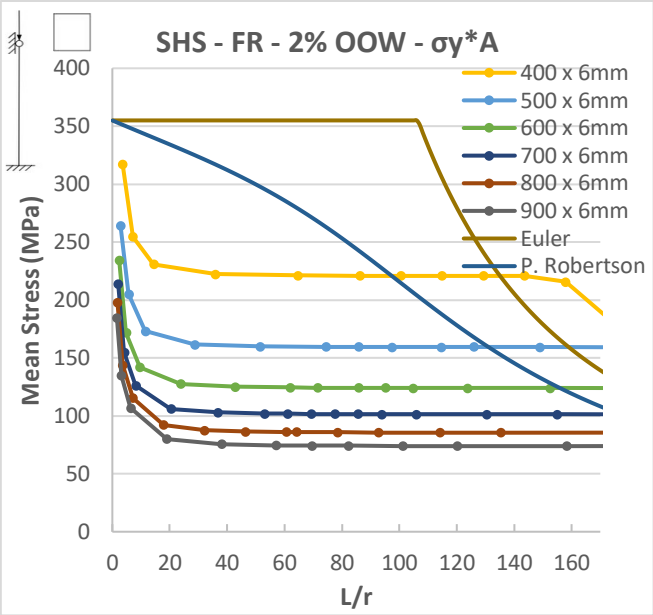

Figure 79: Local buckling zone of 2% out of width Class 4 SHS, fixed roller with axial force only

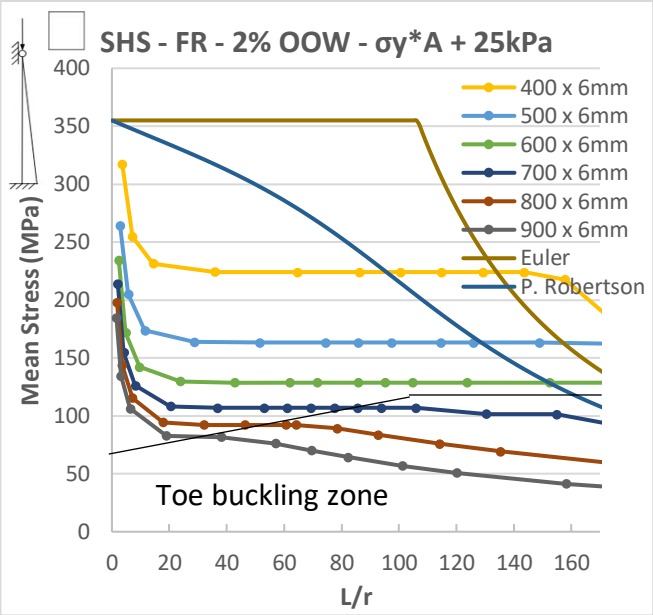

Figure 80: Local buckling zone of 2% out of width Class 4 SHS, fixed roller, with axial force and internal pressure

For D/t ratios greater than 116 and L/r ratios greater than 30, a new local buckling mode is seen when internal pressures are included. This mode is noticed at the toe of the member for both boundary conditions.

The buckling mode is influenced by the magnitude of the internal pressure as the mean stress decreases with increasing L/r ratios. The remaining buckling modes match that of the perfect models.

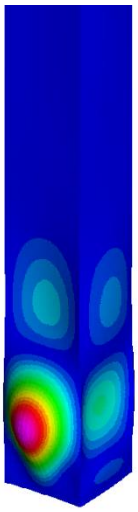

Figure 81: Toe buckling zone for out of width SHS

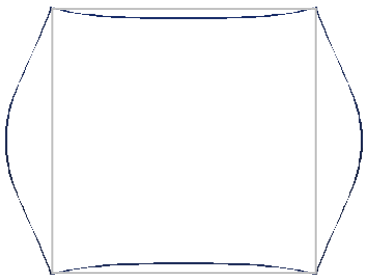

Figure 82: Cross-section of toe buckling zone for out of width SHS

Discussion

The circular and square hollow sections revealed a dispersion of results consistent with the classification of sections theory. Class 1 to 3 sections behaved as predicted whereas class 4 sections showed partially unpredicted results, more so with an increase in the diameter or width-to-thickness ratio.

For very stocky members, the initial out of straightness had a negligible effect and the failure occurred by local buckling. For slender members, the lower bound curve was close to the elastic critical stress (σ_{cr}) curve. Initial out of diameter or width showed a significant strength reduction for circular sections and a strength enhancement for square sections.

Circular Hollow Section

Figure 28 to Figure 31 show the mean stress curves for the perfect CHS for both boundary conditions and load cases. Figure 35 and Figure 36 show an enlargement of the local buckling zone for the class 4 sections. Some observations were drawn from the results.

It was found that all buckling stresses for the perfect and perturbed models were above the yield stress of structural steel. The global buckling curve for all models approached the Euler Bernoulli curve with a high coefficient of determination (R-Squared).

The order of sine waves noticed in the local buckling mode shapes consistently decreased with a decrease in the length (L) to radius of gyration (r) ratio and increased with an increase in diameter (D) to thickness (t) ratio.

The internal pressure had little influence on the local buckling mode shape for Class 1 to 3 sections. However, the position of the occurrence of local buckling along the length of the member shifted toward the zone of lower internal pressure, which marginally increased the mean stress needed to induce buckling.

For the Class 4 sections, where the D/t ratio was greater than or equal to 83, the internal pressure increased the members strength and form increasing consistency in the mode shape with increasing D/t ratios. This can be seen in Figure 36 where the 900mmx6mm section shows 8 sine waves for all L/r values in the local buckling zone. It can also be seen that the curves flatten with increasing D/t ratios.

It was found that an increase in the K value due to different boundary conditions reduced the local buckling range, which is consistent with theoretical equations. The boundary conditions have a marginal effect on the local buckling mode shapes. In cases where the mode shape transitions from a higher order of sine waves to a lower order, the higher K value transitions sooner (at a lower L/r ratio).

Out of Straightness

Figure 37 to Figure 40 show the mean stress curves for the circular sections perturbed along their length for both boundary conditions and load cases. Figure 41 and Figure 42 show an enlargement of the local buckling zone for the class 4 sections.

It was found that the global buckling mode shapes matched the perfect models. The local buckling modes were similar with a few exceptions. The mean stress required for elastic buckling was marginally less than the perfect models. Not all mode shapes were clear, some D/t ratios showed both local and global buckling deformations.

For the lower L/r ratios, the number of sine waves in the locally buckled state matched the perfect models, but the amplitude of the waves was greater on the shorter side of the curved member. A new local buckling mode shape was noticed for larger L/r ratios when internal pressures were included. This was noticed on the shorter side of the member. These are short crippling type waves that propel at the centre to upper half for D/t ratios greater than 100 and L/r ratios less than 27. For the same range of D/t ratios, when L/r is greater than 27 the crippling mode occurs at the toe of the element. It was noticed that the toe crippling mode was only present in the fixed roller boundary condition.

At higher L/r ratios for the fixed roller boundary condition only, the crippling occurred at the end of the element containing the fixed boundary condition. This was also the end containing the highest value in internal wall pressure.

For D/t ratios less than 83, a peak drop in strength of 1% was found when compared to the perfect models. Strength reductions of 6% to 12% were seen for D/t ratios ranging from 100 to 150. This was consistent for both boundary conditions, since the strength reduction was in the local buckling zone.

Out of Diameter

Two sine wave counts along the circumference of the member were investigated. The circular sections with perturbations of six sine waves were weaker than the sections with four.

Figure 47 to Figure 50 show the mean stress curves for the circular sections perturbed with four sine waves along their circumference, Figure 53 to Figure 56 show that of the six wave perturbation. Figure 51, Figure 52, Figure 57, and Figure 58 show an enlargement of the local buckling zone for the perturbed class 4 sections.

It was found that the mode shapes conformed to the initial perturbation shape for most L/r ratios when internal pressures were included. For the axial only load case, the mode shape predominantly revealed a collapse of the section with two sine wave counts. This forms the shape of an oval. The internal pressures locked up the walls of the element forcing it to displace more similarly to the initial perturbed shape.

A strength reduction due to the perturbation by four and six sine waves was noticed for all simulations. For four sine waves, the peak strength reduction percentage ranged from 5.7% for class 1 sections to 18.3% for class 3 sections. Little influence from boundary conditions or internal pressure was noticed.

For class 4 sections, the peak strength reduction percentage ranged linearly from 29.7% at D/t = 67 to 49.6% at D/t = 150. The change in boundary condition or inclusion of internal pressure made a difference of up to 1% which was deemed negligible.

For six sine waves, the peak strength reduction percentage ranged linearly from 3.3% for class 1 sections to 16.6% for class 3 sections. Similar to a four sine wave perturbation, no influence from boundary conditions or internal pressure was noticed.

For the class 4 sections, the peak strength reduction percentage ranged linearly from 34% at D/t = 67 to 60% at D/t = 150. The change in boundary condition or inclusion of internal pressure made a difference of up to 1% which was deemed negligible. However, the internal pressure stiffened the walls of the element, making its local buckled mode shape more like the initially perturbed section.

Square Hollow Section (SHS)

Figure 59 to Figure 63 show the mean stress curves for the perfect SHS for both boundary conditions and load cases. Figure 66 and Figure 67 show an enlargement of the local buckling zone for the class 4 sections.

It was found that all buckling stresses for Class 1 to 3 sections were above the yield stress of structural steel. All buckling stresses for Class 4 sections were below the yield stress of structural steel, where the mean stress tended towards 80MPa for the larger width-to-thickness ratios. The global buckling curve of the perfect models approached the Euler Bernoulli curve with a high coefficient of determination (R-Squared).

The local buckling mode shape resembled the half sine wave for all width (W) to thickness ratios. The boundary conditions had a negligible effect on the eigenvectors of the local buckling zone. The boundary conditions reduce the local buckling range with an increase in K value, which is consistent with theoretical equations

The internal pressure marginally increases the eigenvalue for all W/t and L/r ratios. A typical condition was found, like that seen with the circular sections, where the internal pressure shifted the local buckling modes into the upper half where the hydrostatic pressure is lower. This shift of buckling zone is seen throughout the dataset and seems to be the reason for the slight increase in strength.

Out of Straightness

Figure 68 to Figure 71 show the mean stress curves of the square sections perturbed along their length for both boundary conditions and load cases. The local buckling mode shapes matched the perfect models.

The mean stress required for global buckling was higher than the perfect models. The experiments showed that for all W/t ratios, the initially curved element could withstand a larger axial force than the perfect element could. As the L/r ratio increased, the amplitude of the half-sine concave and convex displacement were greater on the shorter side of the member. The shorter length elements felt higher stresses and were the initiation element of the buckled state.

When studying the global buckling mode shape, the element did not buckle in the direction of the initial out of straightness.

Out of Width

Figure 75 to Figure 78 show the mean stress curves for the CHS's perturbed along the width of the member for both boundary conditions and load cases. Figure 79 and Figure 80 show an enlargement of the local buckling zone for the class 4 sections.

The assumption was initially made that all section geometries perturbed to their local buckling mode shape would see an amplified shape and a strength reduction. In the out of width test set, the models were perturbed in this way to validate this assumption. However, this assumption proved to be incorrect for all W/t ratios. The local and global buckling mode shapes matched the perfect models but were stronger.

For large W/t and L/r ratios under the fixed roller boundary condition, a new local buckling mode occurred at the toe of the member, when internal pressures were applied. This resembled a type of elephant foot buckling that would be seen in circular tanks with large D/t ratios.

Conclusion

A mesh building algorithm was developed to include perfect and imperfect geometries in a finite element analysis of hollow sections under the axial only and combined axial and internal pressure load cases. Out of straightness and cross-sectional perturbations were set to exceed design code limits. A linear buckling analysis was run where the extracted eigenvalues and eigenvectors were reported.

A dataset consisting of two boundary conditions and two load cases for a perfect model set and two perturbed model set types was performed, once convergence was accepted. This amounted to 684 simulations of square hollow sections and 1152 simulations of circular hollow sections.

The finite element solution for both the circular and square sections showed a strong correlation to the Euler buckling curve. The inclusion of an internal pressure resulted in a more consistent local buckling mode shape across multiple length to radius of gyration ratios.

For both the circular and square sections, section classification theory was found to be consistent in that all class 1 to 3 sections saw buckling above the yield point of steel. The class 4 square sections buckled well below the yield point while all circular sections collapsed above the yield point.

For circular sections, the internal pressure placed the shell in hoop tension, creating a stress stiffing effect, where a noticeable increase in strength was gained. Since the circular section can respond to the internal pressure in pure tension, it is strengthened. A difference in local buckling mode shape between the axial only and axial and internal pressure load case was noticed in the class 4 circular sections only.

It was found that the worst-case of perturbation strength reduction was when the initial diameter was perturbed by multiple sine waves along the circumference. For all class 4 sections, six sine waves along the circumference resulted in the largest strength reduction. A reduction in strength of up to 60% was recorded. The internal pressure had negligible effect on class 1 to 3 sections.

When the circular members where tested with an initial out of straightness a crippling mode shape was seen on the shorter face of the member. This was first seen at the centre of the element for both boundary conditions. However, at larger slenderness, it was noticed that a toe crippling mode was present in the fixed roller boundary condition only.

However, this was not true for square hollow sections. The perfect mesh was weaker than the perturbed mesh for most local and global buckling modes. The internal pressure had a negligible effect in strength for most length to radius of gyration ratios. A strength reduction was seen with a larger width to thickness and length to radius of gyration ratios when cross-sectional perturbation was considered. This was seen at the toe of the member for both load cases.

Like that of the circular sections, the square sections saw a shift in the local buckling zone to the upper half or the member when internal pressures were included. When amplifying the buckled

mode shape of the perfect model, the assumption that this perturbation is the most severe in reducing the buckling factor for all section geometries is false.

A small difference in the magnitude of the critical buckling stress is seen with a double in the magnitude of the internal pressure. It was shown that an increase in the magnitude of the internal pressure would reveal a similar critical buckling stress but at a slightly lower pressure zone. The variance in pressure simply due to height showed a shift in the buckling zone to lower pressure zones. An increase in internal pressure did not introduce a new buckling mode, instead a more perfect correlation was seen with the theoretical curves.

For both the square and circular sections, the out of straightness theoretical curves showed no benefit as all class 1 to 3 sections revealed buckling strengths greater than the Euler curve and yield stress point.

Suggestions for Future Work

- For curved circular hollow sections, does the local buckling/crippling position occur at the toe of the element for the fixed boundary condition only at all slenderness ratios greater than 150? Does the magnitude of the out of straightness effect this nature?

- Why does six sine waves along the circumference of the perturbed circular section result in the largest strength reduction? Is this consistent with much larger D/t ratios?

- The perturbed models for the square hollow sections show an increase in local and global buckling strength with all perturbations described. Will physical testing support this?

- Other perturbations could be investigated to find reductions in the local and global buckling strengths for square hollow sections. An initially twisted element could encourage antisymmetric sway in the opposite faces resulting in a possible reduction in the global buckling strength. A lopsided cross-section could encourage local and global buckling as a result of the reduction in the second moment of inertia in one axis.

- A geometric and/or material non-linear analysis (second-order analysis) together with a buckling analysis could be used to validate this result set. Could a larger strength reduction in circular hollow sections be seen with this more complex analysis?

- Will structural materials with a higher or lower elasticity be able to draw similar conclusions?

References

1993-1-6, E. (2007). *Design of steel structures.* European Standard: EUROPEAN COMMITTEE FOR STANDARDIZATION.

Al-Shareef, N. (2018). Impact of Holes on the Buckling of RHS Steel Column. *Journal of University of Babylon*, Vol. (26), No. (5).

Arbocz, j., & Babcock, C. (1969). The Effect of General Imperfections on the Buckling of Cylindrical Shells. *Journal of Applied Mechanics*, 28-38.

Dow, M., & Peterson, J. (1960). Bending and compression tests of pressurized ring-stiffened cylinders. *NASA TN D-360*.

Eurocode-3. (2005). *Design of steel structures - Part 1-1: General rules and rules for buildings.*

F AA Crane, J. A. (1997). *Selection and Use of Engineering Materials, 3rd Edition.* Oxford: Butterworth-Heinemann.

Flugge, W. (1932). Die Stabilitat der Kreiszylinderschale. *Ingenieur Archiv 3*, 436-506.

Fung, Y., & Sechler, E. (1957). Buckling of thin-walled circular cylinders under axial compression and internal pressure. *Journal of Aeronaut*, 351-356.

Harris, L., Suer, H., & Skene, T. (1957). The stability of thin-walled unstiffened circular cylinders under axial compression including the effects of internal pressure. *Journal of Aeronaut*, 587-596.

Hutchinson, J., Tennyson, R., & Muggeridge, D. (1971). Effect of a Local Axisymmetric Imperfection on the Buckling Behavior of a Circular Cylindrical Shell under Axial Compression. *AIAA Journal*, 48-52.

ISO-657-14. (2000). *Hot-finished structural hollow sections - dimensions and sectional properties.* International Standard: ISO 657-14.

Lo, H., Crate, H., & Schwartz, E. (1950). Buckling of thin-walled cylinder under axial compression and internal pressure. *Journal of Aeronaut*, 351-356.

Microsoft. (2019). Microsoft Excel. United States Of America.

R.C. Coates, M. C. (1988). *Structural Analysis. Third Edition.* London: Chapman & Hall.

Seifi, R. (2016). Effects of internal pressure on bending buckling of imperfect functionally graded thin cylinders. *Composite Structures 157*.

Sergev, S., & Walton, D. (1962). *Strength of pressurized columns.* Washington: University of Washington.

Strand7. (2014). *Finite Element Analysis Sysytem* (2.4.6 ed.). Sydney: Strand7 Pty Ltd.

Tsien, H., & Karman, T. V. (1941). The buckling of thin cylindrical shells under axial compression. *Journal of Aeronaut*, 303-312.

Wan, C., & Donnel, L. (1950). Effect of imperfections on buckling of thin cylinders and columns under axial compression. *Journal or Applied Mechanics*, 73-88.

Weaver, P. (2000). Design of laminated composite shells under axial compression. *Composites Part B*, 669-679.